

TOPICAL REVIEW • **OPEN ACCESS**

## Recent progress in laser texturing of battery materials: a review of tuning electrochemical performances, related material development, and prospects for large-scale manufacturing

To cite this article: Wilhelm Pfleging 2021 *Int. J. Extrem. Manuf.* 3 012002

View the [article online](#) for updates and enhancements.

## Topical Review

# Recent progress in laser texturing of battery materials: a review of tuning electrochemical performances, related material development, and prospects for large-scale manufacturing

Wilhelm Pfleging 

Institute for Applied Materials - Applied Materials Physics, Karlsruhe Institute of Technology, P.O. Box 3640, Karlsruhe 76021, Germany

E-mail: [wilhelm.pfleging@kit.edu](mailto:wilhelm.pfleging@kit.edu)

Received 27 July 2020, revised 19 August 2020

Accepted for publication 15 November 2020

Published 8 December 2020



CrossMark

## Abstract

Traditional electrode manufacturing for lithium-ion batteries is well established, reliable, and has already reached high processing speeds and improvements in production costs. For modern electric vehicles, however, the need for batteries with high gravimetric and volumetric energy densities at cell level is increasing; and new production concepts are required for this purpose. During the last decade, laser processing of battery materials emerged as a promising processing tool for either improving manufacturing flexibility and product reliability or enhancing battery performances. Laser cutting and welding already reached a high level of maturity and it is obvious that in the near future they will become frequently implemented in battery production lines. This review focuses on laser texturing of electrode materials due to its high potential for significantly enhancing battery performances beyond state-of-the-art. Technical approaches and processing strategies for new electrode architectures and concepts will be presented and discussed with regard to energy and power density requirements. The boost of electrochemical performances due to laser texturing of energy storage materials is currently proven at the laboratory scale. However, promising developments in high-power, ultrafast laser technology may push laser structuring of batteries to the next technical readiness level soon. For demonstration in pilot lines adapted to future cell production, process upscaling regarding footprint area and processing speed are the main issues as well as the economic aspects with regards to CapEx amortization and the benefits resulting from the next generation battery. This review begins with an introduction of the three-dimensional battery and thick film concept, made possible by laser texturing. Laser processing of electrode components, namely current



Original content from this work may be used under the terms of the [Creative Commons Attribution 3.0 licence](https://creativecommons.org/licenses/by/3.0/). Any further distribution of this work must maintain attribution to the author(s) and the title of the work, journal citation and DOI.

collectors, anodes, and cathodes will be presented. Different types of electrode architectures, such as holes, grids, and lines, were generated; their impact on battery performances are illustrated. The usage of high-energy materials, which are on the threshold of commercialization, is highlighted. Battery performance increase is triggered by controlling lithium-ion diffusion kinetics in liquid electrolyte filled porous electrodes. This review concludes with a discussion of various laser parameter tasks for process upscaling in a new type of extreme manufacturing.

**Keywords:** laser structuring, lithium-ion battery, electrode architecture, 3D battery, cell performance, upscaling

(Some figures may appear in colour only in the online journal)

## 1. Introduction

Laser processes for battery materials have different mature levels and can be roughly divided in two types: laser welding and laser cutting. The former type of laser processes has already achieved a technical readiness level of 8 or 9. Related laser systems are qualified or already system proven in industrial environments. Laser cutting can be applied to separators and electrodes. However the current focus relates to electrode cutting. For pouch cell designs, complete electrodes must be cut at high speeds that match the coating speed, which is in the range of 25–50 m min<sup>-1</sup> [1]. Laser cutting has to realize a throughput of at least one to two electrodes per second, which in turn requires a scanning speed of 1–2 m s<sup>-1</sup> [2]. Partial cutting is also used to divide broad coating sheets in half (slitting) or for a separate the current collector from the coated sheet by exposing the current collector tap contact (notching).

Besides conventional welding (e.g. for prismatic cells), laser welding is also used to join electrode layers (e.g. electrode-to-tap joining, tap-to-tap joining, and tap-to-busbar joining). Laser welding with high power fiber laser systems can produce complete battery modules that reach the capacities and cell voltages (e.g. 400 V or 800 V) required for electrical vehicles [3]. The main issue lies designing appropriate clamping elements to ensure close mechanical contact between the joining partners [4]. It was found that laser welding of dissimilar materials, such as CuZn37 sheets on the negative pole of 26650 lithium-ion cylinder cells, is superior to ultrasonic welding and resistance spot welding in terms of the resulting electrical contact resistance and the tensile strength achieved [5]. Deep penetration or keyhole welding seems appropriate for achieving a suitable mechanical strength between the cell terminal and busbar. However, accounting for possible spatter issues is essential.

Welding of aluminum–copper tap contacts and laser welding in pulse overlap using high-frequency local modulation (‘wobbling’) was demonstrated to be industrially reliable; while the depth and width of the weld seams were adjustable in the micrometer range [6]. The battery modules, that power Tesla vehicles consisting of cylindrical cells types or BMWi3 vehicles consisting of prismatic cells, are assembled by using laser welding with wobbling process strategy. So far, laser welding is the most established laser process in battery manufacturing.

The second type of laser process is significantly more sophisticated due to the fact that a direct impact onto the electrochemical properties is expected to push battery performances beyond state-of-the-art technology. This process is based on laser ablation, or modification of composite electrode materials, which is a relatively new manufacturing approach and research topic [7]. A few years ago, research groups in Germany, China, Japan, and Korea started working on this new topic [7–10]. Therefore, laser structuring and modification of electrodes have a technical readiness level below 5 (i.e. the technology is on an experimental level of proof of concept or in the process of being validated under laboratory conditions). However, for future battery development this type of laser process has a great potential to play a significant role in overcoming the engineering challenges of state-of-the-art batteries by merging the three-dimensional electrode and thick film electrode concepts.

Laser processing of electrodes can be related to different parts of electrodes with different objectives regarding tuning the final cell performance. Electrodes of commercially available high-energy or high-power lithium-ion batteries are multimaterial systems consisting of a composite layer, which is deposited via slot-die coating or tape casting on thin current collector foils made of copper (anode) and aluminum (cathode) with thicknesses of about 6–10 μm and 15–20 μm, respectively. In general the cathode side determines the amount of available lithium (i.e. the full cell capacity). The cathode side can be described as a composite material made of an active material (e.g. LiNi<sub>x</sub>Mn<sub>y</sub>Co<sub>z</sub>O<sub>2</sub> with  $x + y + z = 1$ ), a binder (e.g. polyvinylidene difluoride, (PVDF)), carbon black (e.g. TIMCAL), and other additives (figure 1). Carbon black is used to form a network with high electrical conductivity between the particles and the current collector. The binder provides the mechanical integrity necessary to adhere the active layer to the metallic substrate. The calendaring process reduces the porosity of the composite electrode but enhances the particle-particle contact, as shown in figure 1.

The conventional anode is made of graphite and can store up to one lithium atom per six carbon atoms (LiC<sub>6</sub>) and is intercalated in between the respective graphene layers. To avoid lithium plating, the absolute capacity of the anode side is slightly oversized, which is indicated by a cell balancing value (i.e. anode capacity divided by cathode capacity) in the range of 1.1–1.3. In summary, laser texturing has different

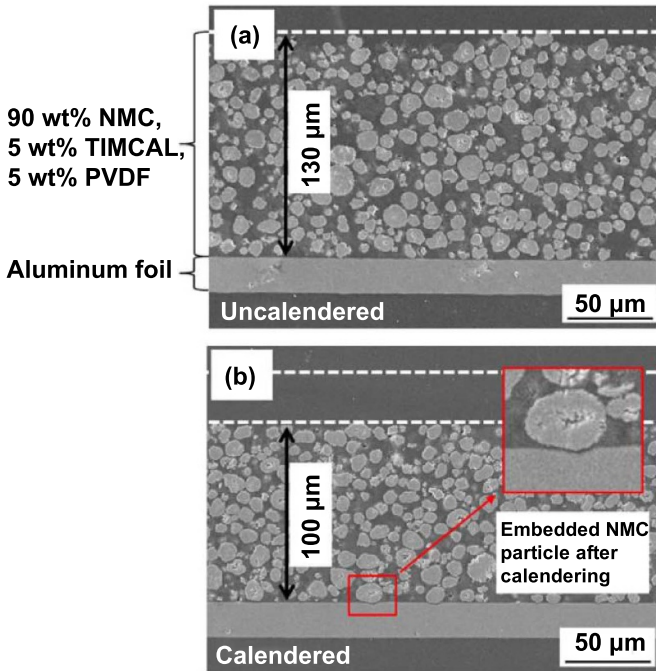


**Figure 1.** Scanning electron microscope (SEM) images of uncalendered and calendered NMC-111 cathodes in cross sectional view; (a) uncalendered electrode (thickness of  $130 \pm 6 \mu\text{m}$ ); (b) calendered electrode (thickness of  $100 \pm 3 \mu\text{m}$ ). The inset illustrates NMC-111 pressed into the aluminum substrate due to calendaring [11].

application opportunities regarding tuning of the electrochemical performance. It can be applied to each part of the multimaterial electrode system, such as the modification and structuring (e.g. drilling, nano-patterning) of the current collector surfaces, modification and selective ablation of the composite electrode surfaces, and structuring of entire composite electrodes down to the current collector [12].

However, a detailed knowledge about the microscopic processes inside composite electrodes and the overall cell system is necessary for enhancing and controlling electrochemical performances via laser texturing. The lithium concentration gradients in liquid electrolytes along the composite electrode induce diffusion of lithium inside the electrolyte. The lithium-ion diffusion kinetics inside the electrolyte filled pores, the charge transfer processes during lithiation and delithiation of active material, the lithium concentration gradients in liquid electrolyte along the composite electrode, and the resulting overpotentials need to be considered in detail.

Overpotentials  $\eta_i$  in lithium-ion batteries have different sources, which lower the cell voltage ( $U$ ) in comparison to the steady-state voltage ( $U_0$ ) which is determined by the Nernst equation under the thermodynamic equilibrium state [13]:

$$U = U_0 + \sum_i \eta_i. \quad (1)$$

$\eta_i$  can represent ohmic resistance, resistance due to ionic transfer through solid electrolyte interface (SEI) layer, charge

transfer resistance, charge double layer capacity, and the concentration overpotentials [14].

Laser processing of electrodes can now provide new strategies to reduce overpotentials  $\eta_i$ . The diffusion overpotential in liquid-electrolyte soaked electrodes arises from the limited diffusion capabilities of lithium in materials with low porosity ( $p$ ) and high tortuosity ( $\tau$ ). The resulting diffusion polarization in the electrodes is attributed to lithium-ion concentration gradients, which is primarily controlled by an effective diffusion coefficient ( $D_{eff}$ ) of lithium in liquid electrolytes [15]. The common definition of the 3D geometrical tortuosity for a porous material is:

$$D_{eff} = \frac{p}{\tau} D_{el}. \quad (2)$$

$D_{el}$  describes the diffusion coefficient of lithium-ions in free electrolytes. The parameter ( $p$ ) is the volumetric porosity of the porous material. The resulting concentration gradient of lithium salt in the electrolyte is enforced by high current rates at high-power operations (i.e. high C-rates during charging or discharging operation). The term ‘C-rate’ can be introduced as follows: A C-rate of 2 C or 3 C corresponds to an electrical current which is necessary to charge/discharge a battery in 1/2 or 1/3 of an hour, respectively. It is quite obvious achieving a high effective diffusivity requires a low tortuosity value. Under optimized conditions, the tortuosity ( $\tau$ ) reaches values near  $\tau = 1$ . Microscopically, this corresponds to a high-aspect-ratio line texture enabling ideally straight and parallel diffusion pathways perpendicularly oriented to the current collector surface. It seems likely that laser structuring of composite electrodes will lead to an artificial porosity and a reduced tortuosity in the thick film electrodes (i.e. an enhanced effective diffusion coefficient ( $D_{eff}$ ) of lithium-ions in the liquid electrolyte) embedded in the porous composite electrode. Therefore, a reduced value of tortuosity can be reached in 3D structured composite electrodes, leading to an enhanced effective lithium-ion diffusion. By choosing capillary structures, such as lines or grid patterns down to the current collector [16] instead of blind borings, one can couple the effect of a boost in diffusivity, described by equation (2), with the effect of accelerated and homogenized wetting of composite electrodes with liquid electrolytes; which can further improve overall reaction efficiency.

At this point, it is important to note that the use of liquid electrolytes for lithium-ion battery (LIB) technology is still state-of-the-art. Thin-film batteries and 3D-micro batteries using solid-state electrolytes are designed for medical or micro-electromechanical system devices and cannot deliver the required energy density for any type of electric vehicles (xEVs). To close this gap, all-solid-state batteries (figure 2) are under ongoing development [17]. Besides requiring further technologically developments, which is a main topic of research groups worldwide [18, 19], another issue is upscaling the process and the inherent challenges to provide the necessary ionic conductivity and stability. So far, all-solid-state batteries cannot provide the required current capability, energy/power density, or cycling stability. Therefore, LIBs with porous electrodes that are filled with liquid electrolytes

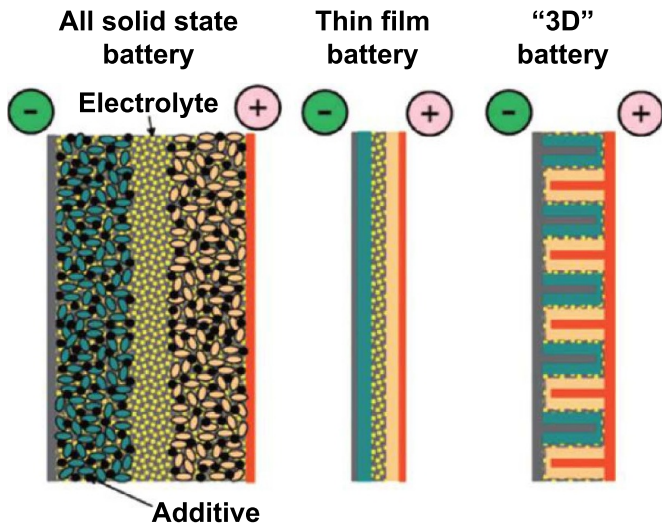


**Figure 2.** A schematic representation of different battery configurations using solid electrolytes (yellow). Current collectors are depicted in grey (negative) and orange (positive), and active materials in green (anode) and beige (cathode), respectively [17].

are still state-of-the-art and will remain so at least for the next decade.

### 1.1. 3D battery concept

What is the benefit of a 3D battery in comparison to a conventional 2D approach with planar electrodes? Besides a decreased overall tortuosity, an increased active surface area should shorten lithium-ion diffusion pathways. The charge transfer resistance will decrease, and a reduction of mechanical tension due to volume expansion and contraction during lithiation and delithiation is expected to increase cycle lifetime. These benefits can be derived from the general 3D battery concept, which was introduced by Long *et al* [20] for micro-scaled batteries (figure 2, scheme on the right): ‘The general strategy... is to design cell structures that maximize power and energy density yet maintain short ion transport distances... A 3D matrix of electrodes... is necessary to meet both the requirements of short transport lengths and large energy capacity.’ This 3D battery concept is primarily applied to micro-batteries with applications in micro- and nano-electromechanical systems (MEMS/NEMS) technology [21]. The design and fabrication of 3D electrodes have become increasingly important in battery systems. Besides laser structuring, advanced 3D printing technologies such as laser-induced forward transfer (LIFT) [22], have promising potential for applications in 3D structured electrodes due to their high design flexibility and capacity for forming complex structures [23]. Pröll *et al* printed a lithium-manganese-oxide-based thick-film electrode (thickness: 50–60  $\mu\text{m}$ ) [24] using the LIFT technique. Overall, the electrochemical performance of the thick-film electrodes could be significantly tuned to higher power operation by combining the LIFT process with ultrafast laser structuring to further increase the active surface area.

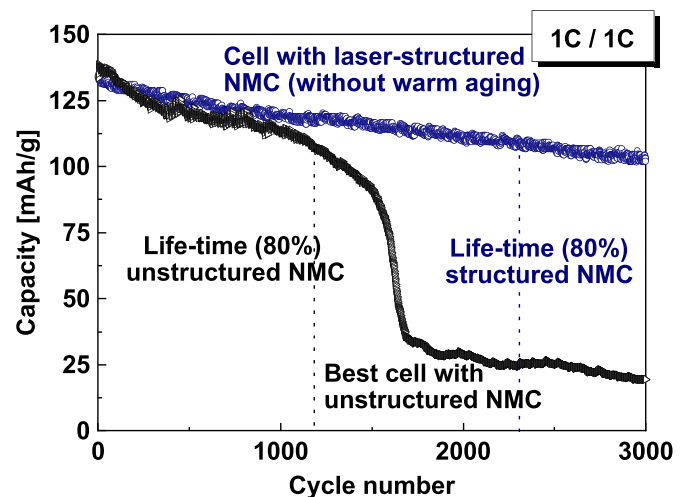


**Figure 3.** Specific discharge capacities of pouch cells with structured and unstructured NMC-111; reproduced from [7].

Cells with structured electrodes show enhanced high-rate capabilities during charging and discharging. They also possess high potential for applications in high-power energy storage devices. About 6 years ago, one of the first publications about laser structured (LS) electrodes demonstrated the capability of 3D structured electrodes for batteries in pouch cell design (i.e. ones with large footprint area) [16]. This work demonstrated for the first time the feasibility of large-scale laser structuring of state-of-the-art composite electrodes and unique improvements on cell lifetime in comparison to cells with unstructured electrodes due to a tremendous improvement in the wetting of structured electrodes with liquid electrolyte (figure 3). After 10 000 cycles, cells with structured electrodes maintain 60% of their initial capacity while cells with unstructured electrodes show a sudden drop in capacity (‘sudden death’) and only reach 1573 cycles for a remaining capacity of 60% [7].

The lack of ‘sudden death’ behavior as a function of cycle numbers for cells with structured electrodes becomes even more astonishing when taking into account that the pouch cells with structured electrodes went to electrochemical cycling directly after the electrolyte filling process without any so called ‘warm aging’, which is required for standard cells to guarantee a sufficient wetting of the electrodes and separator material with liquid electrolyte. A tremendous wetting takes place in structured cells with electrodes, which leads to a sudden drop in the ohmic resistance of the overall cell, reported in [16].

Accelerated electrolyte wetting prevents the warm aging process, including the associated costs for a vacuum, storage space, and logistics. The significant potential of laser processing technology regarding a further reduction of production costs was already discussed in [7]. Laser texturing of ultra-thick-film electrodes can reduce the manufacturing costs of batteries by 20%–30%, besides improving cell lifetime and cycling performance; which means reaching a higher cost efficiency for a more sophisticated product in comparison to the state-of-the-art.

**Table 1.** List of design concepts for pushing state-of-the-art lithium-ion batteries towards next generation.

Concepts	Objectives	Challenges
Mass loading	Energy	Coating, rate capability, overpotential, upscaling
Wetting	Lifetime, safety	Homogeneity, reliability
Material	Energy	Chemical and mechanical stability, volume change, safety, lifetime
3D battery	Power, energy	Processing, upscaling

Table 1 lists different types of technical measures, which show a high potential for reducing the gap in energy density between the material level and cell level, which is typically a factor of four [7]. It is recommended to merge the aforementioned concepts with the use of advanced high-energy materials (material concept) and ultra-thick-film electrodes (mass loading concept) to ensure a high areal capacity and low amount of inactive material. However, these concepts face serious challenges, such as upscaling issues, mechanical instability due to volume expansion, and the formation of overpotentials during electrochemical cycling, see equation (1). To indicate the relevance of introducing laser texturing in battery manufacturing, a short survey of current research activities in the field of new materials and mass loading concept is given in the following sections.

### 1.2. Material concept

State-of-the-art LIBs use  $\text{LiNi}_x\text{Mn}_y\text{Co}_z\text{O}_2$  (NMC) with  $x = y = z = 1/3$  (NMC-111 as active materials on the cathode side) and artificial or natural graphite (C) on anode side. NMC-111 provides a practical specific capacity of  $160 \text{ mA h g}^{-1}$  [25] while graphite intercalates Li-ions with a specific capacity in the range of  $320\text{--}372 \text{ mA h g}^{-1}$ . These values can be calculated using the Faraday law under the assumption that NMC-111 can extract of about 60% of Li within a voltage window of 3.0–4.2 V while in graphite six carbons can theoretically intercalate one lithium leading to  $372 \text{ mA h g}^{-1}$ .

One way to increase the energy density of state-of-the-art NMC-111/graphite batteries is to introduce new active materials on the cathode and anode sides. The current trend in battery manufacturing industry involves increasing the nickel (Ni) content in NMC, which corresponds to an increase in the specific capacity due to the fact that the oxidation of  $\text{Ni}^{2+}$  to  $\text{Ni}^{4+}$  during charging is the main process during delithiation of the cathode material [26]. Table 2 shows different types of NMC materials with their respective specific practical capacities. Following this list, NMC-811 ( $\text{LiNi}_x\text{Mn}_y\text{Co}_z\text{O}_2$  with  $x = 0.8, y = z = 0.1$ ) appears to be the most promising cathode material with a practical specific capacity of  $215 \text{ mA h g}^{-1}$ , which is about 30% higher than the capacity of NMC-111.

**Table 2.** Specific capacity of different types of  $\text{LiNi}_x\text{Mn}_y\text{Co}_z\text{O}_2$  (NMC) with varying Ni content for a voltage window of 3–4.2 V. Data were extracted from [25].

Type of NMC	$\text{LiNi}_x\text{Mn}_y\text{Co}_z\text{O}_2$ ( $x + y + z = 1$ )	Discharge capacity
NMC 811	$\text{LiNi}_{0.8}\text{Mn}_{0.1}\text{Co}_{0.1}\text{O}_2$	$215 \text{ mA h g}^{-1}$
NMC 622	$\text{LiNi}_{0.6}\text{Mn}_{0.2}\text{Co}_{0.2}\text{O}_2$	$198 \text{ mA h g}^{-1}$
NMC532	$\text{LiNi}_{0.5}\text{Mn}_{0.3}\text{Co}_{0.2}\text{O}_2$	$170 \text{ mA h g}^{-1}$
NMC 442	$\text{LiNi}_{0.42}\text{Mn}_{0.42}\text{Co}_{0.16}\text{O}_2$	$163 \text{ mA h g}^{-1}$
NMC 111	$\text{LiNi}_{0.33}\text{Mn}_{0.33}\text{Co}_{0.33}\text{O}_2$	$160 \text{ mA h g}^{-1}$

With increasing nickel content, lithium nickel manganese cobalt oxide tends to form oxygen at elevated voltages due to reduced material stability, which is worse regarding safety and capacity stability [27]. However, recent progress in material development and coating technology encourages battery manufacturers to replace NMC-111 with NMC-622. It seems that NMC-811 will almost certainly succeed NMC-622 as the industry-standard cathode material. Battery manufacturers intend to replace graphite on the anode side with silicon/graphite composite anodes. Silicon (Si) can provide a capacity of  $3579 \text{ mA h g}^{-1}$  at room temperature [28]. Due to the fact that the Si volume changes about 370% [29] during lithiation, it became more useful to mix nano-sized Si particles of a diameter of 150 nm or less with micro-sized graphite particles. These Si/C anodes can reach specific capacities of  $\sim 540 \text{ mA h g}^{-1}$  for a composition of Si (5 wt%) and graphite (90 wt%). The amount of Si will be further increased in future anodes.

It can be concluded that manufacturers of future LIBs will combine nickel-rich lithium nickel manganese cobalt oxide (NMC-622 or NMC-811) cathodes with silicon/graphite anodes. In the classification of LIB cell chemistries these are so-called ‘generation 2b’ and ‘generation 3b (Gen-3b)’ cells. While the latter cell type uses high-energy NMC thick-film electrodes with high-mass loading (see next chapter) or high-voltage spinel cathode materials [30]. Silicon/graphite composites are expected to be the dominant anode materials in Gen-3b batteries. At present, optimized LIB cells of generation 1 and 2a (cathode: NMC-111 or  $\text{LiFePO}_4$  (LFP); anode: carbon or graphite) are the core technology for xEVs. Given the lead time from R&D on battery materials to their actual incorporation in large-scale production, these generations—and incremental improvements to them—are expected to remain the chemistry of choice for at least the next decade [30].

### 1.3. Mass loading concept

The specific energy ( $E_A$ ) per area ( $A$ ) increases with the active material layer thickness and the mass load ( $\text{mg cm}^{-2}$ ) of the cathodes and respective anodes. In the case of compact 2D electrode thin layers (figure 2, scheme in the middle), an increase in electrode layer thickness ( $L_E$ ) leads to a decrease in specific power ( $P_A$ ) due to restricted lithium diffusion in the solid thin-film. Fick’s laws of diffusion describe the intercalation of lithium in the electrode. The lithium-ion transport along

the layer thickness ( $L_E$ ) is described by the diffusion coefficient  $D_{Li}$  ( $\text{cm}^2 \text{s}^{-1}$ ), which determines the shortest time ( $\tau_{0.5}$ ) in which 50% of the lithium-ions are re-intercalated into the cathode (i.e. 50% depth of discharge (DoD) is reached) [31]:

$$\begin{aligned} \tau_{0.5} &\approx \frac{L_E^2}{3D_{Li}} \\ P_A &\approx \frac{0.5E_A}{\tau} \approx \frac{3E_AD_{Li}}{2L_E^2}. \end{aligned} \quad (3)$$

The maximum power that can be extracted decreases with the square of the layer thickness ( $L_E$ ) and linearly with the lithium diffusion coefficient in the electrodes limiting the energy and power of the cell. To overcome these limitations, the compact and dense electrode material is replaced by a thick but porous composite electrode film (figure 1).

In the lithium-ion cells for high-energy applications, the electrodes, anodes, and cathodes, are formed from slurries with active material powders, binders, solvents, and additives which are applied to current collector foils [32, 33]. The thick-film electrodes have a porosity between 30% and 50% in order to allow liquid electrolyte to penetrate through the composite film down to the current collector. The liquid electrolyte contained in the pores enables additional pathways for the lithium-ion conduction. The conductive additives, typically acetylene black, improve the electrical conductivity to the surface of the active particles, where the redox reaction occurs. The homogeneous wetting of the entire electrode with liquid electrolyte is necessary in order to achieve sufficient lithium-ion diffusion kinetics in the entire lithium-ion cell. Dry areas, representing areas of high impedance, do not contribute to the capacity of the cell and are a possible starting point for chemical degradation and accelerated cell aging. Therefore, the wetting process is a key issue and also cost-intensive in battery production [34, 35]. State-of-the-art LIBs typically use composite NMC-111 cathodes with film thicknesses in the range of  $50 \mu\text{m}$  [35].

For commercial cells, it is common to reduce binder and carbon black in electrodes to further increase the energy density. This leads to a high amount (up to 96 wt%) of active material in the coating. Another approach is to increase the layer thickness of the composite electrodes, which saves inactive material and ultimately reduces the volume and mass of metallic current collectors (e.g. aluminum for the cathode and copper for the anode) and separator materials. A thicker cathode and anode would mean that the number of electrode sheets and separator foils would decrease for a given capacity (e.g. 52 Ah [35]). In addition, fewer process steps would be required for pouch cell production, which leads to an increased throughput and improved cost efficiency.

The mass loading or thick-film concept is about increasing the electrode layer thickness and the active mass deposit in order to achieve a higher gravimetric and volumetric energy density for the entire cell (figure 4). Material costs can be reduced by using fewer inactive materials (i.e. current collector and separator). The data for a commercial 52 Ah cell were extracted from Wood *et al* [35]. The electrode stack

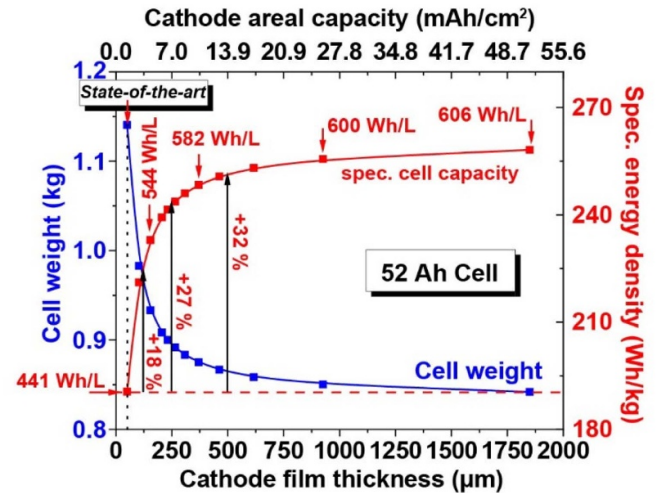


**Figure 4.** Cell weight, gravimetric and volumetric energy density on cell level as function of film thickness and cathode areal capacity for a 52 Ah cell (electrode footprint  $21 \times 24 \text{ cm}^2$ ). Graphs were calculated from state-of-the-art data of 52 Ah ( $50 \mu\text{m}$  cathode thickness) extracted from [35].

begins and ends with a single-side-coated anode. The standard cell has an NMC-111 electrode layer thicknesses of  $50 \mu\text{m}$  with an areal capacity of  $1.39 \text{ mA h cm}^{-2}$ .

For NMC-111 layer thicknesses from  $50 \mu\text{m}$  up to  $925 \mu\text{m}$ , the resulting gravimetric ( $\text{Wh kg}^{-1}$ ) and volumetric energy density ( $\text{Wh l}^{-1}$ ) for a 52 Ah cell can be estimated as a function of cathode film thickness ( $\mu\text{m}$ ) or respectively the surface capacity ( $\text{mA h cm}^{-2}$ ) assuming an uniform porosity and binder distribution. Based on data of a commercial 52 Ah NMC-111 cell, it is then possible to extrapolate the minimum possible cell weight and maximum possible gravimetric and volumetric energy density (figure 4). A volumetric energy density of  $606 \text{ Wh l}^{-1}$  is reached when the number of double-side coated cathodes in the cell stack decreases from 37 (state-of-the-art approach) to 1, i.e. the multilayer cell stack design merges to a single bi-cell design consisting of one double-side coated cathode in the middle and two outer single-side coated anodes each separated from the center cathode by separator sheets.

With a cathode film thickness of  $125 \mu\text{m}$ ,  $250 \mu\text{m}$ , and  $500 \mu\text{m}$  the specific energy density at cell level can be increased by 18%, 27%, and 32%, respectively. Electrode thicknesses greater than  $100 \mu\text{m}$  can achieve significantly higher specific energy densities at cell level. For NMC-111 and an operating voltage of 3.7 V, the specific capacity of  $160 \text{ mA h g}^{-1}$  (table 2) corresponds to an energy density of  $592 \text{ Wh kg}^{-1}$  at the material level. The energy density at the cell level decreases to  $190 \text{ Wh kg}^{-1}$  due to inactive materials such as binder, current, collector, separator, additives, and electrolytes. Increasing the mass loading of NMC-111 electrodes from state-of-the-art  $1.39 \text{ mA h cm}^{-2}$  to  $10 \text{ mA h cm}^{-2}$  can lead to a 30% increase in energy density ( $\sim 190 \text{ Wh kg}^{-1}$  up to  $250 \text{ Wh kg}^{-1}$ ) at the cell level. This corresponds to a volumetric energy density of  $582 \text{ Wh l}^{-1}$ , indicated in figure 4.

While the energy per area increases with the cathode layer thickness, the power density, or ‘high current capability,’ of compact layers decreases—due to limited lithium-ion diffusion kinetics, analogously to equation (3)—and the layer thickness in composite electrodes increases. Another contribution to elevate overpotential (equation (1)) and influence the high rate capability is the length of the path the lithium-ions travel in liquid electrolyte through the composite porous electrode, which is defined by the film thickness, porosity and tortuosity, see equation (2).

Additionally, the mechanical integrity of the films decreases with increasing layer thickness, and binders can migrate to the electrode surface due to altered drying conditions [36, 37]. The mechanical degradation of the cells results from inherent changes in the volume of electrodes in the battery process. Graphite anodes undergo a volume change of up to 10% during battery operation, which becomes more serious with increasing layer thickness in terms of mechanically induced cell degradation.

A variety of cathode and anode materials have been developed to improve high-rate performance. Reducing the diameter of active material particles to increase the electrochemical surface area and forming three-dimensional structures of anodes and cathodes have also been attempted.

Laser structuring of electrodes can counteract the drawback of implementing ultra-thick-film electrodes in LIBs, namely mechanical stability and high-rate capability. An increased active surface area (i.e. an adapted artificial electrode pore morphology) is suitable to enhance lithium-ion transport in electrolytes, which has a positive effect on capacity retention in a certain range of discharge currents.

## 2. Laser structuring of electrode materials

A single electrode of a high energy battery consists of a thin metallic current collector attached to a porous composite layer. At first, it seems quite reasonable to apply laser surface texturing to the metallic surface in order to increase the adhesion properties of the composite layer. The active material needs good mechanical and electrical contact to the metallic substrate current collector. For a pouch cell, the value of the ohmic resistance should be in the milliohm range. A larger resistivity would have adversely impact overpotential (equation (1)) and the overall cell performance; it would also produce significant ohmic heating at elevated C-rates (high power operation), which could force the battery to enter a thermal runaway scenario. It is obvious that laser texturing of current collectors on micro- and nanometer scale can improve composite layer adhesion and electrochemical performance [7]. Laser texturing of current collectors might be useful for developing new electrode concepts, like the development of 3D hierarchical current collectors for binder-free electrodes, a concept described by Yue *et al* [38]. Hereby, the 3D hierarchical current collector increases the surface area for the deposition of active materials in order to increase the electrodes’ areal capacity. Yamada *et al* recently discussed the important role of current collector foils and its surface properties for future

battery developments [39]. Besides improved film adhesion by mechanical anchoring and reduced ohmic resistance, additional measures that can improve the design of current collectors are the precise adjustment of surface energy and wettability to support the coating process and the chemical passivation of aluminum current collector for enabling the use of environment-friendly, water-based slurries based on high-energy nickel-enriched NMC active material, such as NMC-622 and NMC-811 (table 2).

Texturing of current collectors can lead to some improvement, especially regarding film adhesion, and will become important for high-energy anode materials that show large volume changes during lithiation (charging) and delithiation (discharging). However, regarding the impact on lithium-ion diffusion kinetics, laser texturing applied to porous composite active layers is expected to become more relevant. Therefore, the following sections discuss recent promising research studies related to surface modification, selective material removal, and structuring of cathode and anode material for future battery manufacturing.

### 2.1. Laser ablation for electrode surface layers

In general, reaching the battery lifetime means that only 80% of the initial capacity is left due to nonreversible cell degradation. Electrical vehicles reach their battery lifetimes after 400–3000 cycles. A second life operation (e.g. as a stand-alone energy storage system) might be possible as a function of depth of discharge in the range of 40% to 80% [40]. Finally, recycling batteries is required to guarantee an eco- and environmental-friendly closed loop in modern economy [41]. During recycling, aluminum, copper, and other active materials are manually extracted from discharged and disassembled LIBs. Normally, active material is chemically treated in order to recover cobalt and lithium. Another approach is to directly re-use the active material or apply laser cleaning to the disassembled electrodes, which was proposed by Ramoni *et al* [42]. The purpose of laser cleaning is to remove the so-called SEI. The SEI is a thin layer of about 7–35 nm in thickness, which is formed by the reaction between electrolytes and active material—which occurs during battery cycling on the surface of both electrodes, primarily on the anode but also on the cathode—and leads to an increased internal resistance  $R_{SEI}$  and a loss in active material. Furthermore, the SEI layer on top of the electrodes decreases the surface porosity, which in turn decreases the exchange of liquid electrolyte and increases diffusion polarization  $R_{Diff}$ , especially at high C-rates. The necessary selectivity during laser cleaning means to precisely adjust the laser fluence regarding the ablation threshold  $\varepsilon_{th}$  of the SEI. The ablation rate  $\dot{R}_{SEI}$  per laser pulse can be described by a penetration depth (e.g. the thermal diffusion length  $\delta_w = \sqrt{4\kappa\tau_{Puls}}$ ) and a logarithmic term that includes the applied laser fluence  $\varepsilon$  and the material specific  $\varepsilon_{th}$  [43]:

$$\dot{R}_{SEI} \approx \sqrt{4\kappa\tau_{Puls}} \ln \left( \frac{\varepsilon}{\varepsilon_{th}} \right). \quad (4)$$

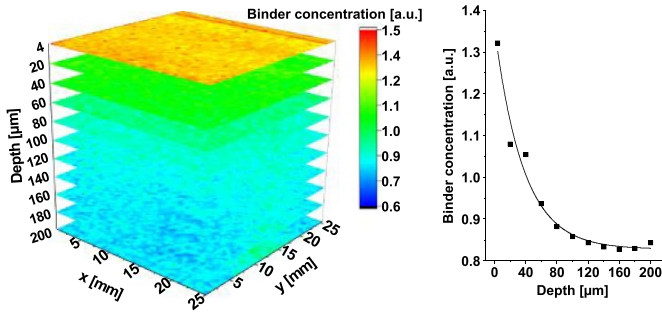


**Figure 5.** Binder distribution in ultra-thick composite NMC-111 electrode (binder: CMC; film thickness: 300  $\mu\text{m}$ ). Binder distribution was measured by LIBS.

Using a laser with a pulse length of 10 ms, as described in [42], will realize a thermal penetration length in the  $\mu\text{m}$  range. It will be quite challenging to selectively remove the SEI from the electrode surface. However, a significant increase in surface porosity on cycled  $\text{LiFePO}_4$  (LFP) could be achieved for laser fluences in the range of 0.3–0.5  $\text{J cm}^{-2}$ .

A laser-assisted surface treatment can also lead to a selective ablation of binder material as recently shown by M. Bolsinger *et al* [44]. One possible method for achieving high volumetric energy densities at cell level significantly above the state-of-the-art value of 441  $\text{Wh l}^{-1}$  (figure 4) is to form a highly compressed electrode layer. Typical cathodes and anodes have electrode porosities in the range of 35%–40%. A calendaring process is subsequently applied to the coating and drying process. Highly compressed electrodes have average porosities (P) significantly below 35%. Values of 20% could be achieved for NMC-111 [44]. the averaged porosity (P) of compressed electrode layers can be estimated by [45]

$$P[\%] = 100\% \left( 1 - \frac{L \left[ \frac{\text{g}}{\text{cm}^2} \right] \left( \sum_i \frac{C_i [\text{wt}\%]}{\rho_i [\text{g cm}^{-3}]} \right)}{D [\mu\text{m}] \cdot 10^{-4}} \right), \quad (5)$$

with mass loading  $L$ , the material densities  $\rho_i$  of the different electrode constituents  $i$ , the portion  $C_i$  of each constituent  $i$ , and the electrode film thickness  $D$ .

Besides a distortion of secondary particles of active materials, sealing the electrode surfaces with a binder material could be observed for highly compressed electrodes. A similar effect was achieved for ultra-thick-film electrodes where a binder migration to the surface was observed as function of the drying conditions [36, 37]. Rapid drying enriches the binder at the electrode surface and leads to its sealing. A typically inhomogeneous binder distribution for those electrodes is shown in figure 5. Hereby, laser-induced breakdown spectroscopy (LIBS) [46] is applied on NMC-111 cathodes made of a water-based slurry. The Na(I) emission line is referred to the respective carboxymethyl cellulose sodium (CMC) binder concentration. These results fit well with EDX investigations for ultra-thick-film graphite anodes (film thickness 400  $\mu\text{m}$ ), which were based on classic N-methyl-2-pyrrolidone-based slurries using PVDF as the binder material [37]. The binder sealing of the electrodes has a negative impact on the electrode wetting with liquid electrolyte.

Selective laser removal of binder (PVDF) and additives (carbon black) was established for ns-laser radiation applying an average laser power  $<1$  W. A low laser line energy is required and a short pulse length helps prevent melting of the active material. For low porosities of 20%–25% and high C-rates  $>2$  C, an enhanced capacity retention could be measured for cells with laser processed NMC-111 electrodes compared to cells with untreated NMC-111 electrodes. Cells with laser processed electrodes with an areal capacity of 2.44–3.658  $\text{mA h cm}^{-2}$  can have specific capacities 24% higher than those of unprocessed cells. However, the benefit of laser processing diminishes or completely vanishes for low C-rates and higher areal capacities (i.e. with increasing film thickness). The effect of an enhanced electrolyte wetting by opening of surface pores becomes less relevant with increasing film thickness due to overall restricted electrolyte wetting.

## 2.2. Cathode structuring

The development of cathodes with 3D architecture is particularly important as the cathode mainly determines the performance of the battery [47].

3D structured cathodes provide superior areal capacities ( $\text{Ah cm}^{-2}$ ) compared to conventional 2D electrodes. However, conventional 3D cathodes (micro-batteries with compact electrodes) have average loading values of 1–3  $\text{mg cm}^{-2}$ , and areal capacities of about 0.1–0.5  $\text{mA h cm}^{-2}$ . Batteries based on compact electrodes barely provide enough energy for high-power applications. Current state-of-the-art 3D technologies are incapable of synthesizing large-scale electrode architectures. Cutting edge technologies, namely printing and laser processing, present two possible technical approaches for realizing the 3D cathode concept with high mass loading into high-power and high-energy applications (figure 6). Printing is a bottom-up approach that enables the formation of flexible electrode designs. Conversely, laser patterning is a top-down technique that removes material from the electrode surface through laser ablation. Periodic surface structures, such as holes, lines, crosses, and free-standing structures, can be produced with high aspect ratios, even at incredibly small feature sizes of approximately 400 nm for thin compact cathodes [48].

Structuring cathodes benefits the discharge process for supporting the lithiation process of the cathode material. The literature presents two main strategies to increase the active surface of composite electrodes by laser ablation. One strategy involves drilling the entire double-side coated electrodes; the other approach ablates grids or line patterns with structure depths down to the current collector.

**2.2.1. Drilling of cathodes.** Recently, it was found that the formation of micrometer-sized holes on the cathodes (i.e. through-holed and non-through-holed cathodes) significantly improves the high-rate charging/discharging performance due to the increased number of paths available for lithium-ion transfer to and from the active materials (LFP and graphite layers). Matsumoto *et al* [9] developed 3D cathodes by drilling the cathode layer and current collectors with a picosecond (ps)

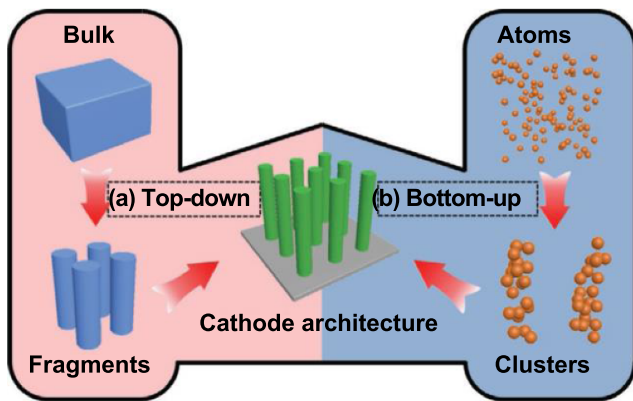


**Figure 6.** Two distinct ways of engineering to realize electrodes with 3D architecture providing a large areal capacity: (a) top-down fabrication via laser patterning and (b) bottom-up fabrication via deposition or printing. Reprinted with permission from [47]. Copyright 2020 John Wiley and Sons.

pulsed laser. The idea was that through-holes accelerate the lithium-ion transfer in the entire cathodes. The through-holed LFP/activated carbon (AC) cathode, in which the LFP and AC layers were coated on each side of an aluminum current collector, and micrometer-sized holes were formed with a ps-laser and the discharging process occurred preferentially on the AC layer. Energy was then transferred from the charged LFP layer to the discharged AC layer with the transfer of lithium-ions through the holes formed in the LFP/AC cathode [9].

Tsuda *et al* used a ps-laser to drill electrodes [49, 50] for so-called unbalanced double-side coated LFP cathodes. The respective layer thicknesses were  $29\ \mu\text{m}$  and  $7\ \mu\text{m}$ , which corresponds to a mass loading of  $3.9\ \text{mg cm}^{-2}$  and  $0.9\ \text{mg cm}^{-2}$ , respectively. Typical hole diameters were  $36\text{--}40\ \mu\text{m}$  while the applied pitch distance was  $167\ \mu\text{m}$ . The purpose of using unbalanced double-side coated cathodes is related to the fact that thin-film electrodes can sustain a higher capacity for high C-rates. Figure 7 shows the experimental data and a schematic illustration of the discharging process using through-holed, non-through-holed, and non-holed unbalanced LFP electrodes. Unbalanced and balanced LFP/LFP cathodes exhibited the same discharge capacities at low C-rates (e.g.  $0.1\ \text{C}$ ) while at high C-rates (e.g.  $5\text{--}20\ \text{C}$ ) the discharge capacity of the balanced cathode was significantly lower than the unbalanced one. The improvement in the discharging performance of the drilled cathodes at high C-rates may result from a facilitated transfer of lithium-ions during discharging through the holes of the LFP electrode. In order to maintain a discharge capacity—at high C-rates and in thick LFP layers—high enough to improve LIB performance, the optimization of the diameter of the holes formed and the number of holes per  $\text{cm}^2$  are major issues for ongoing research.

Figure 7 shows the discharge capacity as a function of the C-rate for full cells composed of through-holed LFP/LFP cathode and two graphite anodes (figure 7(a)), non-through-holed LFP/LFP cathode and two graphite anodes (figure 7(b)), and unstructured LFP/LFP cathode and two graphite anodes

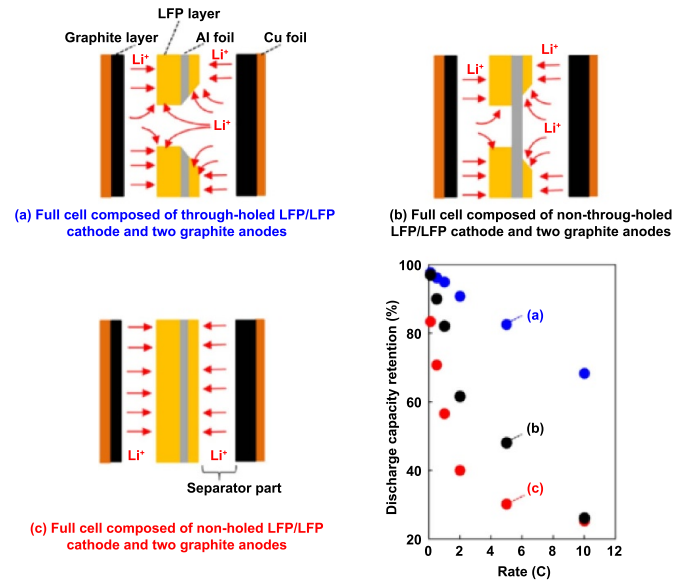


**Figure 7.** Schematic views of full cells in bi-cell design with different types of laser drilled ((a) and (b)) and unstructured (c) unbalanced LFP cathodes and respective discharge capacities as a function of C-rate. Reprinted with permission from [50]. Copyright 2019 The Electrochemical Society of Japan.

(figure 7(c)). In each case, the loading of the two anodes were  $1.7$  and  $0.39\ \text{mg cm}^{-2}$ , respectively [50].

To improve the high rate performance of lithium iron phosphate LFP cathodes, the LFP and AC layers were coated on either side of an aluminum current collector (LFP/AC cathode). The coated current collector was subsequently drilled through with holes with an average diameter of  $18\text{--}23\ \mu\text{m}$  and an opening rate of  $0.44\%\text{--}0.64\%$  by ps-laser ablation in the LFP/AC cathode [48]. Cells manufactured with a perforated LFP/AC cathode and two lithium metal anodes showed a significantly improved high-rate capability at  $50\ \text{C}$  and  $100\ \text{C}$ , which corresponds to a discharge time of  $72\ \text{s}$  and  $36\ \text{s}$ , respectively. The perforated LFP/AC cathode had a far better high-rate performance than both the perforated and unperforated LFP/LFP cathodes. Based on the results, it was found that in a high-rate discharge process, the AC layer is discharged at a higher rate than the LFP layer due to its higher power. Hereby, electrons are transferred—because of the difference in the electrode potential between the AC and the LFP layer—from the charged LFP layer to the discharged AC layer. Simultaneously, the lithium-ions transfer from the AC layer through to the LFP layer via the generated through holes. The formation of through holes in the LFP/AC cathodes leads to an improvement in the charge/discharge capacity and the high-rate capability. However, at high C rates, the LIBs which were described above are not discharged completely at the same time, but the capacity is used up by several discharging steps. Therefore, in order to evaluate the rate performance for the discharging process, discharging was performed by repeating 11 high-rate discharge cycles and one low-rate discharging with a  $5\ \text{min}$  interruption between each discharging process.

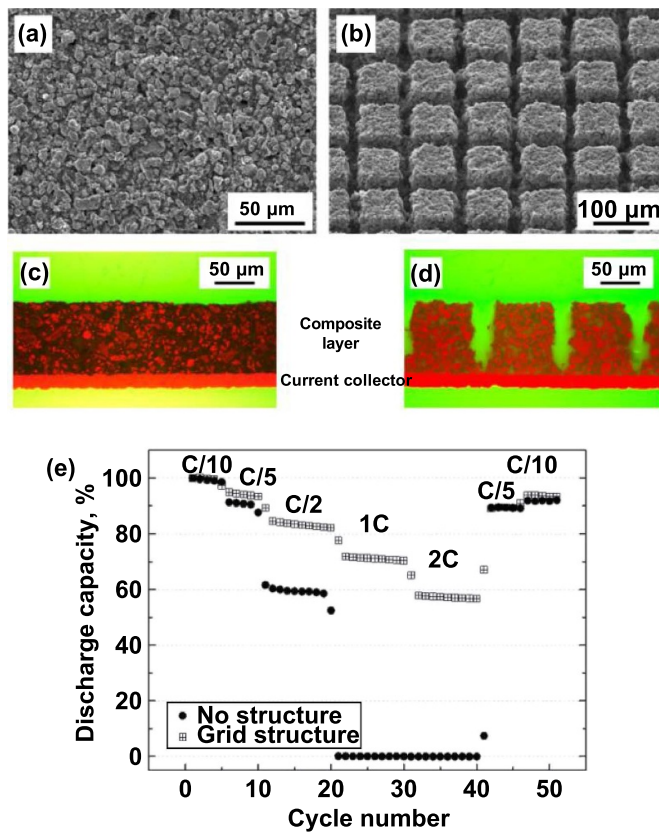


**Figure 8.** Unstructured (a) and (c) and structured (b) and (d) composite LiCoO<sub>2</sub> (LCO) electrode in SEM top view (a) and (b) and microscope cross-sectional view (c) and (d). (e): Normalized discharge capacity as function of cycle number for different C-rates for cells with structured (b) and (d) and unstructured (a) and (c) LCO electrodes [51].

**2.2.2. Cathodes with line or grid pattern.** Laser structuring of cathodes for introducing the 3D battery concept to high-energy applications, namely thick-film composite electrodes, can be easily realized by line or grid structuring (figures 8(a)–(d)), as shown in numerous publications for different types of cathode materials for more than a decade [7, 45, 51].

The advantages of line structure can address upscaling, which will be discussed in chapter 3. However, all the studies that use line or grid patterns for thin-film or composite thick-film cathodes observed a significant improvement in capacity retention, especially at high C-rates, similar to those shown in figure 8(e). Besides the previously mentioned improvement in electrode wetting with liquid electrolyte, improvements in lithium-ion diffusion kinetics were also observed. These improvements are attributed to the increased active surface area (see chapter 2.5 about diffusion kinetics). However, it should be pointed out that structuring of the cathode material is always related to a decrease in areal capacity due to the fact that active mass, carrying the lithium charge, is removed from the electrode. Cathode structuring should be focused on the systems that use ultra-thick-film electrodes (i.e. systems with high areal capacity ( $>4 \text{ mA h cm}^{-2}$ )) or for cells with highly

compacted electrodes with low porosity. In general, a small loss in active mass in the order of 5 wt% should be targeted.

### 2.3. Anode structuring

Structuring of anodes becomes increasingly important for cells to be charged at high C-rates. Especially for electrical vehicles short charging times are required for broad public acceptance. For example, a charging time of 10 min means that the lithiation of anode material is performed at a C-rate of 6 C. Applying high C-rates to state-of-the-art LIBs with graphite anodes will have two major impacts:

- fast reaching of the upper cut-off voltage leading to reductions in charging time and the achieved capacity
- an enforced tendency to initiate lithium plating on the anode side

It is characteristic that the oval-shaped graphite particles in state-of-the-art flake-like graphite material will orient themselves along the graphene diffusion planes parallel to the electrode surface during coating. Additionally the length of the lithium-ion migration path in liquid electrolyte between the flake-like graphite particles is larger than spherical electrode materials, such as the more expensive meso carbon microbeads. Both aspects enhance the diffusion overpotential at high C-rates: the cut-off voltage will be reached sooner and a significant drop in the capacity will occur.

However, besides pure graphite anodes, so-called high-energy silicon or silicon/graphite anodes will become more relevant for future battery systems. Graphite anodes can provide specific capacities of  $372 \text{ mA h g}^{-1}$ , assuming that during lithiation one lithium-ion is assigned to six graphite atoms within the hexagonal graphite structure ( $\text{C}_6\text{Li}$ ). This lithium intercalation process leads to a macroscopic anode volume expansion of about 9%–10%. Recent in-operando x-ray diffraction measurements showed up to 13.2% increases in unit cell volume during lithiation [52].

In terms of further energy density improvements by anode material measurements, there is a general agreement, that the most promising strategy is a stepwise addition of Si to the graphite-based anode material, in the form of Si or SiO<sub>x</sub> (nano-)particles. However, the addition of Si is related to various challenges of Si materials that limit the LIB cell's cycle life, including large volume changes, contact loss, mechanical electrode degradation, instability of the SEI, and loss of active Li during lithiation/delithiation. Currently, Si is used in only a few commercial cells (e.g. Panasonic) in the form of SiO<sub>x</sub> while small amounts of up to 8 wt% are applied [53]. In comparison to graphite anodes, pure Si anodes at room temperature can deliver almost one order of magnitude higher specific capacities of about  $3590 \text{ mA h g}^{-1}$ , which corresponds to  $\text{Li}_{15}\text{Si}_4$  at fully lithiated state [29]. Instead of an intercalation process, an alloying process takes place during lithiation of silicon with volume changes of about 370%. The high volume change during electrochemical cycling may pulverize the silicon particles. Therefore, silicon nano-sized particles are used in order to avoid particle cracking. A simple approach

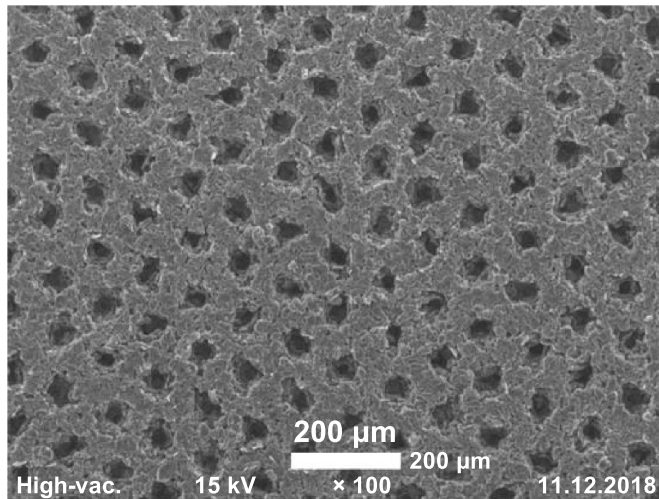


**Figure 9.** SEM image (top view) of a laser-structured graphite anode [56].

for the critical crack length ( $a_c$ ) of Si with fracture toughness ( $K_{Ic}$ ) and elastic limit ( $\sigma$ ) is given by equation (6), resulting from [54].

$$a_c = \frac{2 K_{Ic}^2}{\pi \sigma^2} = \frac{2 (0,751\text{MPa}/\sqrt{\text{m}})^2}{\pi (1,1\text{GPa})^2} = 297\text{nm}. \quad (6)$$

According to this simple estimate, particle sizes above 300 nm must be avoided in order to prevent crack formation and constant SEI formation and thus the decomposition of the electrolyte and the active material. To stabilize the SEI layer, fluoroethylene carbonate and vinylene carbonate are added to the liquid electrolyte [55]. The Si particles lose their electrical contact with the surrounding particles due to volume contraction; the electrode layer can detach from the current conductor. Significant improvements to lifetime and cycle stability present a major challenge for the commercialization of silicon-based anode materials. Introducing free-standing structures with high adhesion to the current collector should counteract mechanical degradation. The focus is on the development of suitable structuring processes and their transmission and scaling for battery production. Meanwhile, silicon/graphite composite anodes are the most promising types of anodes in terms of transferability to commercial systems, especially those with low Si contents around 5–10 wt% [53].

The following subchapters present different femtosecond (fs) laser generated patterns in anode material and their impact on capacity retention, lithium plating, and mechanical degradation.

**2.3.1. Holes pattern.** Habedank *et al* [8] proposed drilling hexagonal arranged holes in graphite anodes, as shown in figure 9.

The lateral distance of the holes was set to 100  $\mu\text{m}$ . The reported mass-loss was 5%–10% [56] and the ablation

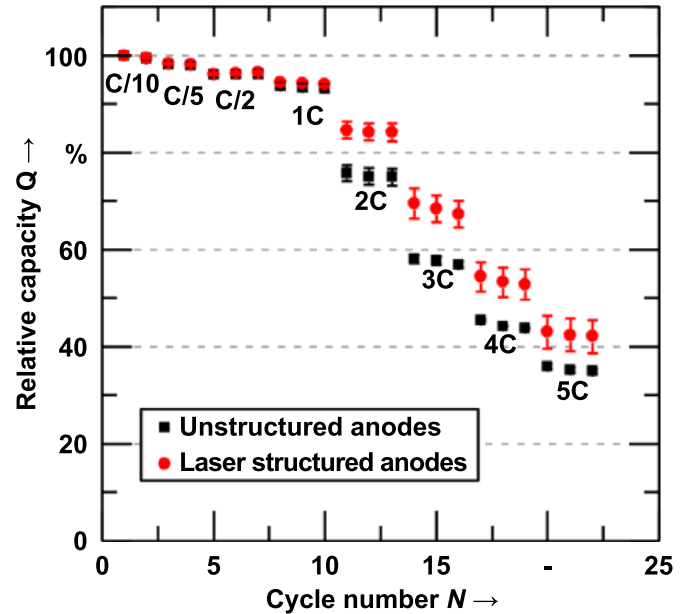


**Figure 10.** Normalized discharge capacities of Li-ion coin cells with LS and unstructured anodes. Reprinted with permission from [8]. Copyright 2018 Laser Institute of America.

depth was in the order of the electrode-film thickness. Sub-nanosecond (ns), ps-, and fs-laser ablation was investigated [8, 56, 57]. The conical-shaped holes had a diameter of 25–35  $\mu\text{m}$ . ps-Laser drilling was performed with an average laser power of 10 W, a laser pulse repetition rate of 1.2 MHz, a pulse energy of 8.33  $\mu\text{J}$ , and an irradiation time of 0.6 ms per hole [56]. An average hole density of  $10^4 \text{ cm}^{-3}$  and an average electrode footprint area of 504  $\text{cm}^2$  for a 52 Ah cell [35] resulted in  $5.04 \times 10^6$  holes per electrode and a processing time of 50 min per electrode. However, process upscaling is a main issue when transferring this approach to industrial manufacturing of cells for high-energy applications.

Figure 10 shows the capacity improvement for NMC/C full coin cells (capacity of 3.9 mA h) with LS anodes as a function of the C-rate. Capacity retention improvements were achieved for C-rates larger than 1 C. The strongest impact was obtained for high-power operations and C-rates of about 3 C where cells with LS anodes provided a 20% higher capacity compared to cells with unstructured anodes. The observed effect was attributed to reduced diffusion overpotential due to improved lithium-ion transport in liquid electrolyte-soaked anodes. The laser-generated openings in the flake-like graphite particle packages significantly shortened the lithium-ion pathways in the composite electrode.

Fast-charging and charging at low temperatures are the main reasons for lithium-plating on graphite anodes. The diffusion of lithium in graphite is a temperature-dependent process and declines with decreasing temperature. Electrolyte viscosity also decreases with decreasing temperature. Both effects limit the possible lithiation rate in graphite particles, and metal lithium deposition takes place on the particle surfaces, especially on the anode surface.

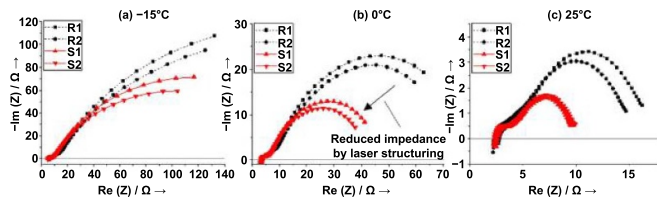


**Figure 11.** EIS in a measurement frequency range of 100 kHz to 1 Hz, recorded at an open circuit voltage of 3.7 V and temperatures of (a)  $-15^{\circ}\text{C}$ , (b)  $0^{\circ}\text{C}$ , and (c)  $25^{\circ}\text{C}$  for laser-structured (S1, S2) and reference cells (R1, R2). Due to the high impedance at low temperatures of about  $-15^{\circ}\text{C}$ , the second semi-circle is only visible partly in the applied frequency regime [57].

Hadedank *et al* [57] showed that charging cells with ps-LS anodes become increasingly beneficial with decreasing temperatures compared to cells with unstructured anodes. Overpotentials attributed to charge transfer and diffusion (i.e. lithium-ion transport in liquid electrolyte) can be reduced. Electrochemical impedance spectroscopy (EIS) revealed that the charge transfer ( $R_{ct}$ ), which is attributed to the second semi-cycle (indicated by arrow in figure 11(b)), can be significantly reduced in LS electrodes for all temperatures, see figure 11.

Lithium-plating during fast charging at low temperatures is suppressed in cells with structured anodes, which is attributed to improved kinetics and reduced charge transfer resistance. Critical operating conditions, i.e. charging with C-rates  $\geq 1$  C at an ambient temperature  $\leq 0^{\circ}\text{C}$  become manageable. Lithium-plating and subsequent dendrite formation and cell failure and even thermal run-away can be suppressed using cells with LS graphite anodes.

**2.3.2. Anodes with line or grid pattern.** State-of-the-art graphite anodes show a volume expansion of  $\sim 10\%$ , which is about three times higher than state-of-the-art NMC cathode materials. Line patterns and grid patterns offer an appropriate strategy to counteract those volume expansions and a subsequent deficiency of liquid electrolyte, which is pressed out of the composite anode. Grid and line structures act as capillary structures and electrolyte reservoirs, enabling a rewetting of the porous anode material with liquid electrolyte. Introducing high-energy materials such as silicon or silicon/graphite as a composite anode exacerbates the issue of volume expansion because lithiated silicon has a volume expansion of 300%–400%.

Zheng *et al* [58] compared grid and line structures for silicon/graphite (Si/C) electrodes (figure 12). They concluded that the grid structures were superior to the line structures in terms of isotropic volume expansion and contraction during battery operation. Shi *et al* [59] used *in situ* SEM analysis to study the lithiation of laser line structured Si/C anodes in comparison to unstructured ones and proposed an active mass removal of almost 50% for providing enough space to compensate the huge volume expansion.

The performance of cells with LS graphite or Si/C anodes, both with grid structure and a structure periodicity (‘pitch’)

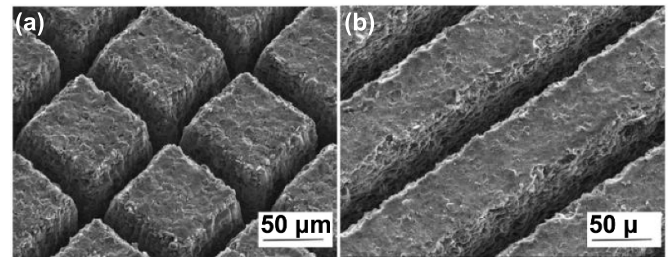


**Figure 12.** SEM of fs-laser generated (a) grid and (b) line structures in silicon/graphite electrodes (Si 20 wt%, graphite 60 wt%, active mass loading  $3.1\text{ mg cm}^{-2}$ , film thickness  $55\text{ }\mu\text{m}$ , line pitch  $100\text{ }\mu\text{m}$ , laser fluence  $0.44\text{ J cm}^{-2}$ , laser scanning speed  $500\text{ mm s}^{-1}$ ). Reprinted with permission from [58]. Copyright 2019 Elsevier.

of  $100\text{ }\mu\text{m}$ , were compared to cells with unstructured electrodes. As shown in figure 13, the structured state-of-the-art graphite electrodes achieved impressive performance results with constant capacity values for low (C/5) and high-power operation (3C) [58]. The initial capacity of Si/C electrodes exceeded  $700\text{ mA h g}^{-1}$ , which is twice the value for standard graphite anodes (figure 13). The capacity retention for all investigated C-rates remained relatively stable in the cells with LS Si/C electrodes. Cells with unstructured electrodes, graphite or Si/C, showed significant capacity fading for C-rate values  $\geq 2\text{C}$  or C/2, respectively. EIS analysis revealed that laser structuring significantly reduced the cell impedance, specifically the charge transfer resistance [58]. This was attributed to a reduced mean tortuosity that facilitated lithium-ion transport and an increased mean porosity which provided a higher surface area for charge transfer. Furthermore, laser structuring of Si/C electrodes prevented wrinkling, which typically occurs due to substantial volume changes in the thin copper current collector foil.

Column structures of physical vapor deposition (PVD) synthesized silicon films provide an intrinsic porosity that can compensate for large volume changes during electrochemical cycling. These films have a thickness of only a few hundred nanometers. Piwko *et al* [60] used successfully ultrafast laser structuring to generate hierarchical micro-/nanostructures with thicknesses ranging from several micrometers up to  $4\text{ }\mu\text{m}$ . The fabricated structures achieved the theoretical capacity of  $3579\text{ mA h g}^{-1}$  and practical anode areal capacities of up to  $7.5\text{ mA h cm}^{-2}$ . Their results suggest that the additional porosity, generated by the laser during lithiation, is filled with active material. It has been demonstrated that the use of laser-structured silicon anodes improves the capacity conservation compared to unstructured ones. They also suppressed current collector wrinkles. However, this approach led to a loss of active material in the range of 40–50 wt%, which led to a corresponding decrease in the areal capacity.

#### 2.4. Thick film electrodes

Thick-film electrodes are extensively investigated as a powerful approach for increasing areal capacity and reducing the amount of inactive material. However, several drawbacks

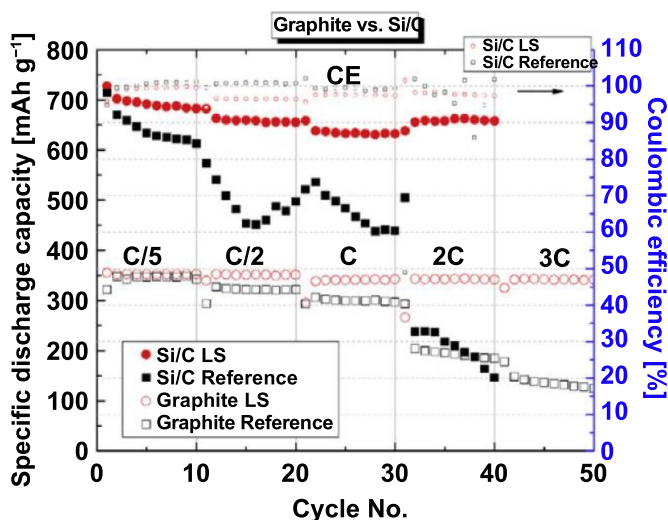


**Figure 13.** Specific discharge capacity and coulombic efficiency for cells with LS and unstructured (reference) graphite and Si/C electrodes (parameters for laser structuring: grid structure, pitch  $100\ \mu\text{m}$ , laser wavelength  $515\ \text{nm}$ , repetition rate  $200\ \text{kHz}$ , laser scan speed  $500\ \text{mm s}^{-1}$ , pulse length  $380\ \text{fs}$ , laser fluence  $0.44\ \text{J cm}^{-2}$ ). Reprinted with permission from [58]. Copyright 2019 Elsevier.

exist, such as changes in binder distribution (figure 5) and significant decreases in high-rate capability. Thick-film electrodes suffer from poor lithium-ion diffusion within the electrode bulk material and increased electronic resistance. The active material close to the current collector surface is used less during electrochemical cycling because it shows the longest lithium-ion diffusion path-length from the active material to the free electrolyte at the electrode surface. In the worst case scenario, the bottom layer might be unchanged during electrochemical cycling at high C-rates. In contrast to the particles attached to the current collector, the active material particles at the electrode/electrolyte surface suffer from the highest electronic resistance.

Thick electrodes result in deterioration of rate capability, severe capacity loss at high current rates, and low capacity retention during long-term cycling despite the increase in areal energy density. As a result, the electrode thickness of most industrially-manufactured LIBs does not exceed a range of  $50\text{--}100\ \mu\text{m}$ . Optimization of electrode porosity is also closely related to the LIB performance. A well-designed electrode should ensure a balance between electrode density, or compaction, and rate capability performance. The severe decline in rate capability observed in low-porosity electrodes at increased current rates results from a spatially heterogeneous electrochemical reaction along the electrode thickness down to the current collector. Typically, the porosity of industrial LIBs is in the range of  $30\%\text{--}50\%$ , depending on the type and thickness of the electrodes.

Park *et al* [60] investigated NMC-622 with a film thickness of  $100\ \mu\text{m}$  and a mass loading of  $28\ \text{mg cm}^{-2}$  compared to standard electrodes with film thickness of  $70\ \mu\text{m}$  and mass loading of  $20\ \text{mg cm}^{-2}$ . Using LIBs to study the change of state of charge (SoC) as a function of the electrode depth and

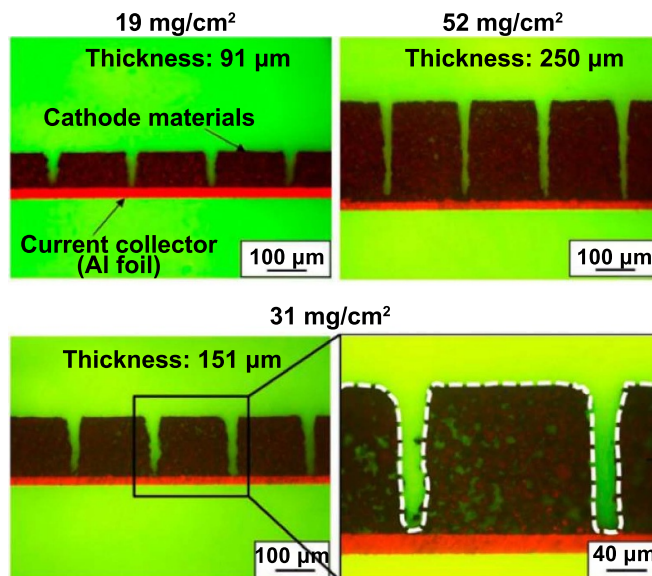


**Figure 14.** Cross sectional view of LS NMC-622 cathodes with different film thickness (laser parameters: wavelength  $1030\ \text{nm}$ , repetition rate  $200\ \text{kHz}$ , scan speed  $500\ \text{mm s}^{-1}$ , average power  $3\ \text{W}$ , pulse length  $380\ \text{fs}$ , pitch distance:  $200\ \mu\text{m}$ ) [45].

cycle number, they identified a change in the lithium concentration along the film thickness, indicating that the bottom layers of the electrode are less involved in the electrochemical process as the number of cycles increases. These lithium-ion concentration gradients are starting points for material degradation and current hot-spot formation in the upper regions of the cathode layers. This study shows that a slight increase in mass loading can have severe impacts on overall cell performance and cell safety.

Park *et al* [10] reported that expanding the lithium-ion diffusion path through laser structuring can compensate for the drawbacks caused by increased electrode thickness or decreased porosity, such as power density drop and low capacity usage range. At low C-rates of  $C/10$ , the unstructured electrodes show a slightly higher areal energy density ( $\text{Wh cm}^{-2}$ ), which is due to the loss of active materials caused by laser ablation. However, the advantage of high-mass loading can be maintained for C-rates equal or above  $C/2$  only for cells with structured electrodes. In other words, cells with LS electrodes can achieve high-energy and high-power operation at the same time while the conventional type of battery production can only fulfill one task.

Zhu *et al* [45] applied the 3D battery concept to NMC-622 electrodes with a thickness of  $250\ \mu\text{m}$  and a mass load of  $52\text{--}54\ \text{mg cm}^{-2}$  (figure 14). Using high aspect ratio fs-laser ablation, Zhu *et al* reduced the active mass loss to  $3\%$  and  $8\%$  for line structures with a pitch distance of  $600\ \mu\text{m}$  and  $200\ \mu\text{m}$ , respectively. Other studies with NMC-111 show that the fs-laser generated mass loss could be reduced to  $6\%$  for a line pitch of  $200\ \mu\text{m}$  and an aspect ratio of  $\sim 13$  [7], refer to figure 20.

Galvanostatic measurements suggest that half-cells with structured NMC-622 electrodes performed better at discharge

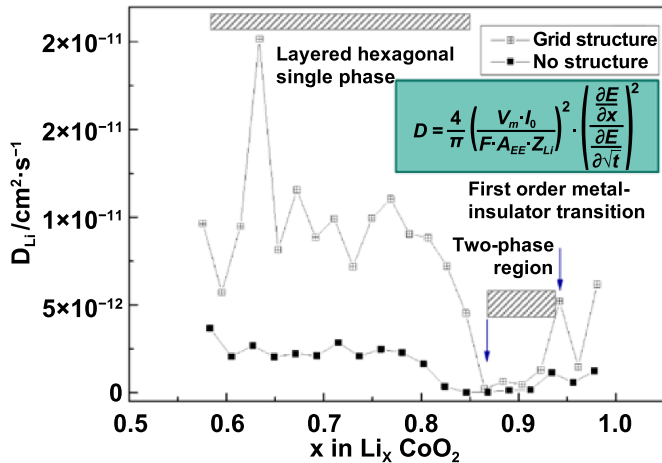


**Figure 15.** Chemical diffusion coefficient of lithium-ions for LS (grid structures, see figure 8) and unstructured composite  $\text{LiCoO}_2$  electrodes as function of SoC [51].

rates of C/2 to 3C. For example, the capacity of cells with NMC-622 and a film thickness of  $250 \mu\text{m}$  exceed the capacity of a corresponding cell with unstructured electrodes for C-rates above C/5. For electrodes with a film thickness of  $151 \mu\text{m}$  and  $250 \mu\text{m}$ , laser-structured cathodes with a line pitch distance of  $200 \mu\text{m}$  offer a  $40 \text{ mA h g}^{-1}$  higher discharge capacity at C/2 and 1C, respectively [45]. With increasing layer thickness, the suitable C-rate for cells with structured electrodes shifts to lower values, i.e. the laser structuring concept becomes more powerful with increasing electrode film thickness.

## 2.5. Diffusion, pathways, and modeling

One main impact of LS 3D electrode architectures is the overall improvement in lithium-ion transport properties within the composite active material. Chemical diffusion coefficients can be used to compare the lithium-ion transport properties of cells with LS and unstructured electrodes. These coefficients can be determined by electrochemical methods, such as cyclic voltammetry (CV) or the galvanostatic intermittent titration technique (GITT). While CV measures the average value of diffusion coefficient [61], GITT provides diffusion coefficient values for each SoC (figure 15) [51].

A threefold reduction in ohmic resistance was detected by measuring the  $IR$  drop (voltage drop across the cell impedance is the product of current  $I$  passing through resistance  $R$ ) as function of SoC [51], which can be assigned to an increase in the electrode surface that is in direct contact with the free liquid electrolyte.

However, from LIBS it became evident that additional lithium-ion diffusion pathways activate in LS electrodes at high-power operation. The sidewalls of free-standing NMC-111 electrode structures show an increased lithium concentration in comparison to the inner part of the so-called micro-pillar model electrodes (figure 16(a)).

A donut-like lithium concentration profile was observed from the top (figure 16(b)), and a tooth-root-like shape was

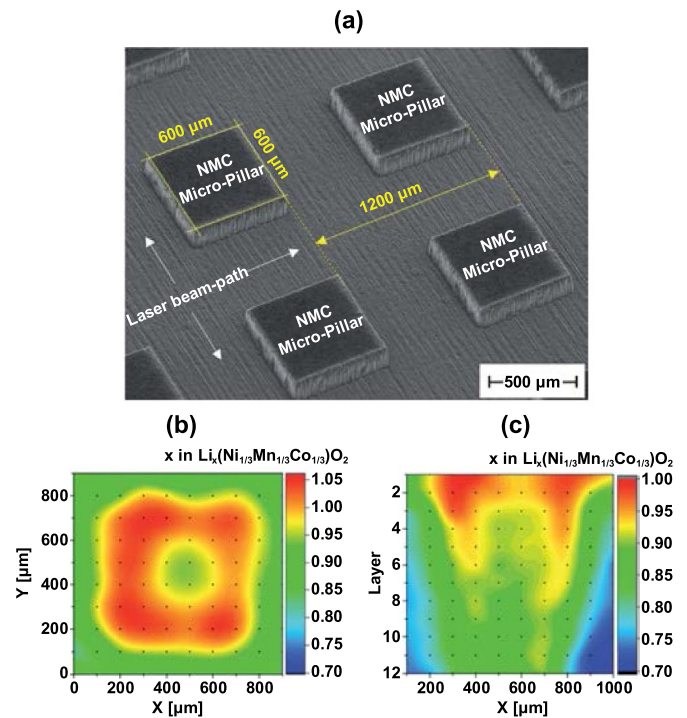


**Figure 16.** (a) SEM (top-view) of a laser-structured NMC-111 thick film model electrode (free-standing micro-pillars, each with size:  $600 \mu\text{m} \times 600 \mu\text{m} \times 100 \mu\text{m}$ ) for subsequent LIBS measurement (post mortem); (b) lithium mapping (top view) of a free-standing micro-pillar, (c) lithium mapping (cross sectional view) micro-pillar after electrochemical characterization (charging/discharging 2C/2C) [46].

observed in the cross section (figure 16(c)). It should be noted that the increase in lithium along the new pathways is not as dramatic as it would be during lithium-plating. The variation in lithium concentration is quite small and occurs within  $x = 0.95 \pm 0.05$  for  $\text{Li}_x(\text{NiMnCo})\text{O}_2$ ; an undesired lithium-plating would lead to significantly greater variation (i.e. around  $x = 1.4$ ), as shown in [46]. The lithium concentration in structured electrodes reaches values close to the stoichiometric composition of NMC-111, which corresponds to the safety aspects required for battery operations (figure 16).

For graphite anodes, the improvement in power performance is even more evident than for cathode materials, which was shown by the high stability in capacity retention for C-rates up to 3 C, as shown in figure 13. This boost in performance can be drawn from the preferential orientation of the graphite flakes, which is parallel to the current collector and perpendicular to the diffusion direction through the electrode. This generates a spatial tortuosity anisotropy and creates particularly long diffusion pathways through the electrode. Due to laser structuring, the preferred diffusion planes come in contact with the free electrolyte, which makes high-power operation possible along the sidewalls of the free-standing micro-pillars, as shown in figure 17. fs-laser ablation has no negative impact on the current collector's topography or the electrochemical performance, namely the diffusion planes of the active material. The laser ablation enables new diffusion possibilities along the sidewall of the free-standing structures

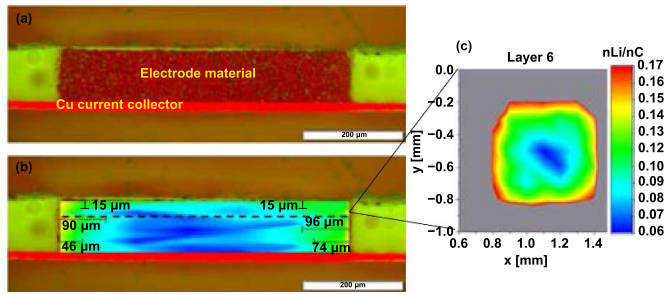


**Figure 17.** Quantitative LIBS measurements for illustration of lithium diffusion pathways in fs-LS graphite anodes: (a) cross sectional microscopic view of free-standing graphite micro-pillar (size:  $600\ \mu\text{m} \times 600\ \mu\text{m} \times 100\ \mu\text{m}$ ); (b) lithium concentration profile in cross sectional view with lithium penetration depths; (c) lithium concentration mapping ( $600\ \mu\text{m} \times 600\ \mu\text{m}$ ) parallel to the surface in a depth of  $38\ \mu\text{m}$  measured from the top of the pillar [62]. The electrode was lithiated at  $0.01\ \text{V}$  by applying a C-rate of  $1\ \text{C}$ .

indicating that no damage of the active material occurs. Concluding from figure 17, the lithium diffusion length from the sidewall in direction to the center of micro-pillar center is  $46\text{--}96\ \mu\text{m}$ . This result led to a design rule for anodes that enable optimum lithium-ion diffusion kinetics for high-power operation. The design rule requires that diameter of the laser generated free-standing structures should be no greater than  $100\text{--}200\ \mu\text{m}$ .

Based on the so-called Newman-like model [63], the electrochemical cell is represented by three 1D domains for anode, separator, and cathode, each characterized by its thickness. In this model, the effective diffusion coefficient  $D_{eff}$ , equation (2), describes the lithium-ion transport in liquid electrolyte within a porous electrode represented by spherical particles. The laser patterning enhances the lithium-ion transport kinetics in the liquid electrolyte. Therefore, the tortuosity ( $\tau$ ) must be adapted to the pore morphology and porosity. The laser-generated pore morphology of the graphite anode enhances lithium-ion transport and reduces the concentration gradients in the electrolyte along the electrode thickness towards the current collector substrate.

Based on mass and charge balance in the solid particles, Butler–Volmer equation can be used to describe the charge transfer kinetics while applying appropriate boundary conditions for mass and charge transfer in the electrolyte and respective interfaces to electrodes and separator. Kraft *et al* [56] recently combined the Newman-like 1D model with 1D radial symmetric active material particles to the p2D model to describe the electrochemical performances of cells with LS anodes. Kraft *et al* showed that the diffusion polarization in the liquid phase is the dominant factor in the anode and mainly influences the overall electrochemical cell performance (figure 18). The structuring process improves the transport in the electrolyte and reduces overpotentials caused by diffusion polarization. A maximum reduction of the anode overpotential by structuring was achieved at  $3\ \text{C}$  in accordance with the experimental data. The maximum capacity retention occurred at a discharge C-rate of  $5\ \text{C}$ , which corresponds to

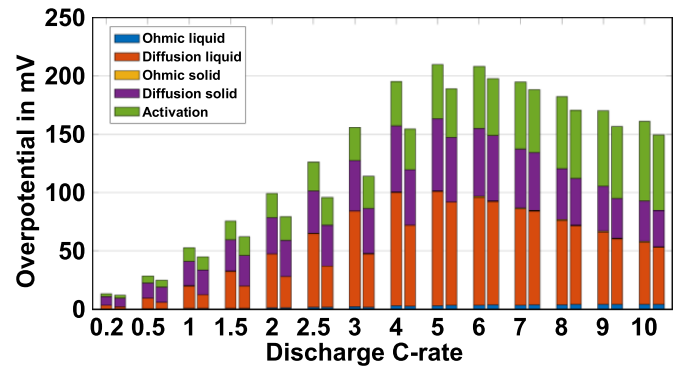


**Figure 18.** Anode overpotentials as a function of C-rate. The laser pattern used for LS anodes is shown in figure 9. Each pair of bars represents data of cells with either unstructured anodes (left bar) or structured anodes (right bar). The different contributions to the overpotential are shown in the legend [56].

a peak in the general liquid diffusion polarization. The effective electrolyte diffusivity, equation (2), is strongly affected by the tortuosity and porosity. High anode tortuosity lowers the effective diffusivity and increases the lithium salt concentration gradients.

### 3. Laser process upscaling

The advantages of introducing laser structuring to battery materials, such as electrodes, current collectors, and separator materials, are evident and clearly proven in several of the research studies mentioned in previous chapters. Industrial flanked projects have already been initiated to develop technical concepts to transfer laser structuring technologies to battery manufacturing [64, 65]. It is a benefit that the dynamic progress in LIB development forces the battery industry to guarantee high-flexibility to enable the transfer of new battery concepts in manufacturing. As a result, the battery manufacturing sector must integrate interchangeable manufacturing modules. One prominent example is laser cutting, which will become more integrated in battery manufacturing. Laser cutting modules, or processing of electrodes, are already developed and commercially available technology for performing slitting, notching, and final electrode cutting [66]. Laser cutting enables high design flexibility and provides an almost maintenance-free technology compared to classic blade cutting or punching technologies. Compared to punching, ns-laser cutting reaches its financial amortization within  $2\text{--}5$  years [67]. However, recent studies using fs-lasers instead of ns-lasers show that improving existing commercial cutting modules could lead to significant advantages, regardless of the type of electrode material [7, 68]. For example, using an fs-laser can entirely suppress droplet formation along the laser cutting kerf in LFP electrodes. Recent progress in the development of industrial reliable, ultrafast laser sources with powers up to  $300\text{--}500\ \text{W}$  illustrates the potential for introducing ultrafast laser processing in battery manufacturing [3, 69, 70]. Laser cutting and laser structuring of electrodes have similar issues in battery material processing regarding processing

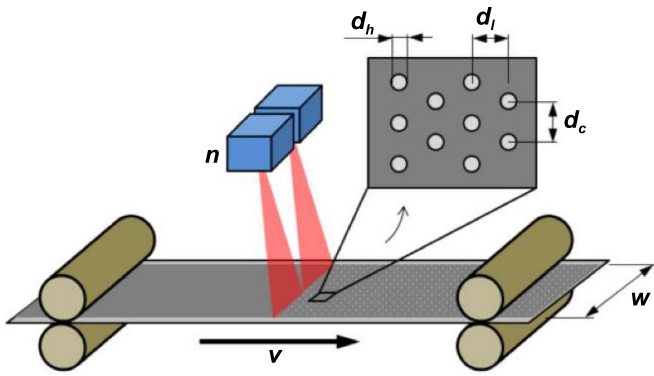


**Figure 19.** Schematic view of a processing concept for high-speed anode laser drilling using multiple laser scanning heads. Reprinted with permission from [65]. Copyright 2020 Laser Institute of America.

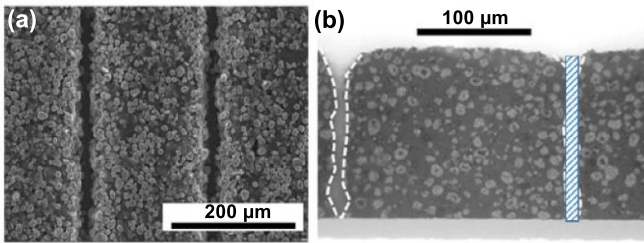


**Figure 20.** SEM images of laser-structured NMC-111 thick-film electrodes. (a) top view and (b) cross-sectional view (hatched area:  $12 \mu\text{m} \times 155 \mu\text{m}$ ) [7].

speed and preventing cross-contamination and particle redepositions along electrode surfaces [66]. While particle redeposition can be controlled by introducing suitable exhaust designs; the processing speed is a crucial factor. Laser cutting of electrodes requires laser scanning speeds of  $1\text{--}4 \text{ m s}^{-1}$ , an average laser power of  $200\text{--}400 \text{ W}$ , and laser repetition rates of up to  $20\text{--}50 \text{ MHz}$  [71, 72] to cut  $1\text{--}2$  large areal electrodes suitable for pouch cell geometries per second. This type of high-speed cutting is necessary due to the electrode coating speed ( $25\text{--}50 \text{ m min}^{-1}$ ). The same boundary condition is given for electrode laser structuring. In [65] a technical scanner solution for precise multi-pass drilling of anode materials with borehole spacing of  $200 \mu\text{m}$  was presented assuming an electrode coating speed of  $20 \text{ m min}^{-1}$ . Laser scanning speeds of  $2312 \text{ m s}^{-1}$ , a laser power of  $462 \text{ W}$ , and six laser drilling passes are listed as assumed parameters for the drilling of anodes materials as shown in figure 9. Figure 19 gives an impression of the laser energy distribution required for multi-beam laser processing to match the high-coating speed.

The laser processes must be examined on surfaces as large as  $30 \times 30 \text{ cm}^2$  to transfer the new electrode concept to production lines and integrate it in roll-to-roll (R2R) processes as well as the damage-free and debris-free processing of active and inactive materials. When upscaling, the process must be optimized in a way that protects the materials from the adverse effects of thermal processes. An important step was the early research in the area of laser processing of thick-film electrodes

using fs-laser radiation in order to avoid thermal impacts by ns lasers [24, 61, 64, 73–79].

Laser-induced material modification by thermal impact could provide starting points for enhanced cell degradation. Therefore, it is essential to suppress or avoid laser-induced active material modification. Previous studies [7, 16] show that for graphite anodes and NMC cathodes the laser-induced material modification by melting or decomposition can be neglected. The laser ablation process is initiated when the binder material decomposes while the rise in temperature rise can be kept below the decomposition and melting temperatures of the respective active material. No drawbacks regarding electrochemical performances could be detected. Conversely, LFP undergoes substantial changes [61]. Applying ns-laser ablation to an LFP active material generated a melt phase, which suggests that ps- or fs-laser processing is required. Finally, it can be stated, ultrafast laser ablation is strongly recommended for preventing thermal damage and realizing of high aspect ratio structures.

The laser structuring process parameters for integration into a battery production line are estimated below. First, it should be noted that channels with a width of  $w = 12 \mu\text{m}$  can be created in electrode materials using ultrafast laser radiation (figure 20). These channels act as capillaries for homogenized wetting with liquid electrolyte. The recommended channel depth for wetting is  $70\%\text{--}100\%$  of the layer thickness [80].

For process upscaling a typical laser beam diameter in scan direction of about  $d_x = 30 \mu\text{m}$  could be used and for a conventional electrode thickness in the range of  $50\text{--}100 \mu\text{m}$  the required laser pulse overlap is in the order of  $N = 10$  for material removal down to the current conductor. In addition, the dimensions sketched in figure 21 with groove spacing  $p$  (‘pitch’) and groove length  $l_x$  should be applied to the formation of the line pattern.

For an electrode coating speed  $V_{B,y}$ , the laser scanning speed  $V_L$  and the laser repetition rate  $\nu_{\text{rep}}$  are calculated as follows:

$$V_L = \frac{l_x}{p} V_{B,y} \tag{7}$$

$$\nu_{\text{rep}} = \frac{N l_x}{d_x p} V_{B,y} \tag{8}$$

The active mass loss  $\eta$  due to the laser structuring results in

$$\eta [\%] = \frac{w}{p} \cdot 100\% \tag{9}$$

For three different groove spacings,  $p = 600 \mu\text{m}$ ,  $1 \text{ mm}$ , and  $2 \text{ mm}$ , the laser repetition rate and the laser scanning speed were calculated as function of the coating speed (figure 22). A laser scanning speed of  $100 \text{ m s}^{-1}$  and a repetition rate of  $33 \text{ MHz}$  result for a coating speed of  $30 \text{ m min}^{-1}$  and a groove pitch of  $p = 1 \text{ mm}$ . The loss of active mass is  $\eta = 1.2\%$ . The latest generation of ultrafast laser sources, namely those with InnoSlab Design [81, 82], with average laser powers of  $300\text{--}500 \text{ W}$  and laser repetition rates up to  $50 \text{ MHz}$  covers this

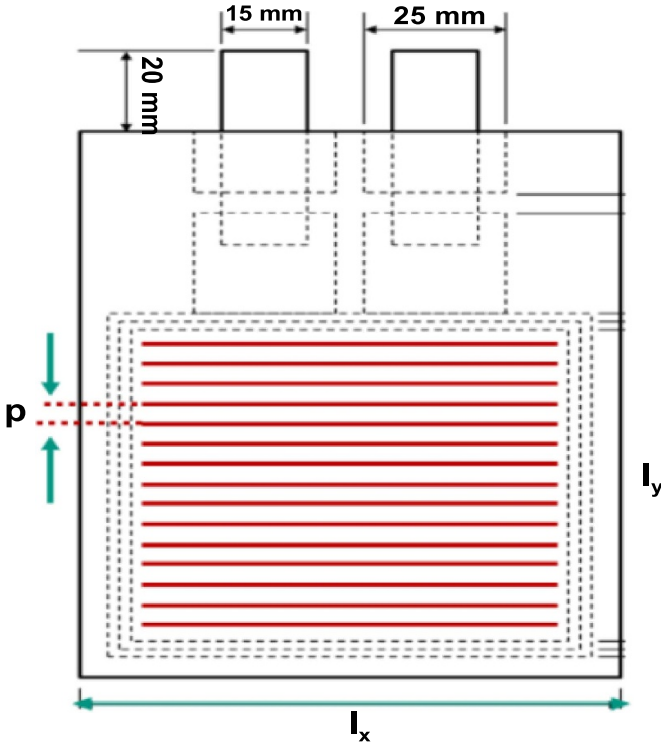


**Figure 21.** Schematic view of laser generated line pattern placed on a pouch cell electrode with line pitch  $p$ , line length  $l_x$  and a rectangular electrode footprint ( $l_x \times l_y$ ).

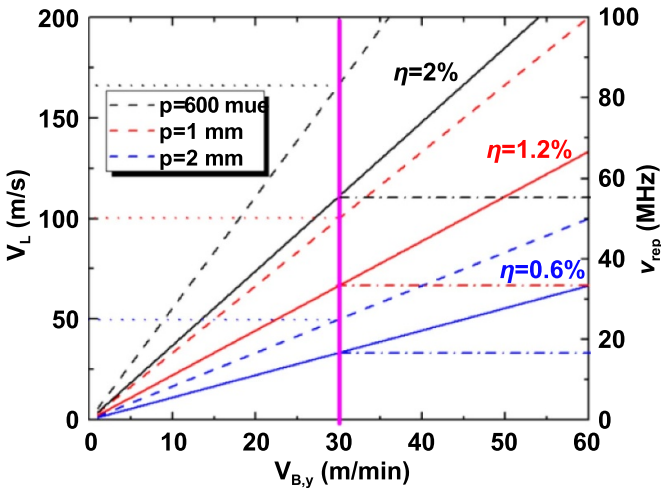


**Figure 22.** Laser scanning speed  $V_L$  and laser repetition rate  $\nu_{rep}$  as a function of electrode coating speed  $V_{B,y}$  calculated from equations (7) and (8), respectively. The active mass loss  $\eta$  from equation (9) was calculated for three different line groove spacings  $p$  (focus diameter  $d_x = 30 \mu\text{m}$ , pulse overlap  $N = 10$ , electrode size in scan direction  $l_x = 20 \text{cm}$ ).

parameter range. The high scanning speeds can be achieved using galvo or polygon scanner systems. Due to the high laser powers, which are technically feasible even in the kW range, it makes sense to carry out an optical splitting of the laser energy for parallel or multispot processing, analogous to technical solutions from laser processing of solar cells [83].

Another aspect that speaks in favor of multi-spot processing is that, following the logarithmic ablation law for Gaussian laser radiation [43], the volume removed per time  $\dot{V}$

$$\dot{V} = P \cdot \frac{1}{2} \cdot \frac{\delta}{\epsilon_0} \cdot \ln^2 \left( \frac{\epsilon_0}{\epsilon_{th}} \right) \quad (10)$$

divided by the mean laser power  $P$  reaches its maximum for

$$\left( \frac{\dot{V}}{P} \right)_{max} = \frac{2 \cdot \delta}{e^2 \cdot \epsilon_{th}} \quad (11)$$

with an optimized repetition rate  $\nu_{rep}$  of

$$\left( \frac{\nu_{rep}}{P} \right)_{opt} = \frac{2}{e^2 \cdot \pi \cdot w_0^2 \cdot \epsilon_{th}} \quad (12)$$

and an optimized energy density of

$$\epsilon_{0,opt} = e^2 \cdot \epsilon_{th} \quad (13)$$

with  $\epsilon_0$  as the pulse peak energy density,  $\epsilon_{th}$  as the energy density of the ablation threshold,  $\delta$  as the energy penetration depth (optical penetration depth or heat penetration depth) and  $P$  as the mean laser power. The optimal energy densities for an efficient removal process are relatively small but 7.4 times greater than the removal threshold. In terms of efficiency, only higher laser powers make sense if multi-spot laser processing for ablation is applied. Finally, using multi-beam processing enables laser scanning speeds that are significantly lower than those derived from figure 22.

Thick-film electrodes will be integrated in the next generation battery concept. Therefore, with increasing film thickness the required laser pulse overlap ( $N$ ), for one pass laser ablation down to the current collector, will increase and the aforementioned technical concept must be adapted to the new situation: a rectangular intensity beam is recommended for each single beam. In the laser scan direction, the laser beam might have an elongation of  $d_y = 200 \mu\text{m}$ . Perpendicular to the scan direction, the beam width ( $d_x$ ) is assumed to be equal to the generated groove width ( $w \approx d_x = 20 \mu\text{m}$ ). The laser pulse overlap is  $N = 60$ , which reflects the conditions for electrode-film thicknesses between 200 and 300  $\mu\text{m}$ . Table 3 provides estimated laser parameter for the multi-beam processing approach using five laser beams and different groove spacings ( $p$ ). These show that the laser structuring process can be scaled to meet the requirements for battery manufacturing process chains. The coating speed ( $V_{B,y}$ ) is the most challenging factor. However, given the recent developments of original equipment manufacturer type fs-laser sources with high power and high repetition rates, the next step of integrating laser processing pilot lines and production lines—with industrial robustness parameters—becomes feasible. This is the logical consequence for the next generation battery, which needs to be capable of handling high energy and high power operations simultaneously.

**Table 3.** Laser parameters for laser structuring of thick film NMC-111 electrodes (required pulse overlap for ablation  $N = 60$ ) in a R2R process (process adapted to coating speed of  $V_{B,y} = 30 \text{ m min}^{-1}$ ) including multi-beam processing (five beams) and beam shaping ( $d_x \times d_y = 20 \times 200 \mu\text{m}^2$ ), electrode size in scan direction  $l_x = 135 \text{ mm}$ .

Parameter (five beams)		Pitch 200 $\mu\text{m}$ (five beams)	Pitch 600 $\mu\text{m}$ (five beams)	Pitch 1 mm (five beams)
Scan speed	$V_L = \frac{l_x}{5p} V_{B,y}$	$68 \text{ m s}^{-1}$	$23 \text{ m s}^{-1}$	$14 \text{ m s}^{-1}$
Repetition rate	$\nu_{rep} = \frac{N}{d_x} \frac{l_x}{5p} V_{B,y}$	$20 \text{ MHz}$	$7 \text{ MHz}$	$4 \text{ MHz}$
Weight loss	$\eta [\%] = \frac{w}{p} \cdot 100$	10%	3%	2%

#### 4. Outlook

Cells containing LS thick-film electrodes for a high energy density and high power operation exhibit excellent battery performances. To achieve 3D anodes and cathodes in commercially available batteries, the mass production of 3D anodes and cathodes is fundamentally required. Laser processes for cutting, annealing, and structuring battery materials show great potential for battery mass production and have been further developed to minimize fabrication costs and increase electrochemical performance and operational lifetime of batteries. It is especially important to develop highly scalable methods by shortening laser processing times.

Future battery production concepts are driven by cost, performance, and quality. Cell and electrode formats and throughput per production line must also be considered in electrode and subsequent cell production. Laser technology can contribute to the following technical goals: increase battery lifetime (>10 000 cycles), reduce charging time (5–10 C), increase energy densities (250–350 Wh  $\text{kg}^{-1}$ ) and power densities (1250–3500 Wh  $\text{kg}^{-1}$ ), and reduce cell costs by at least 20%. In this way, the research results achieved can significantly contribute to improving battery performance and safety as well as reducing manufacturing costs, and thus align with the growing social and economic requirements for mobile and stationary energy storage. The EASE (The European Association for Storage of Energy) and EERA (The European Energy Research Alliance) released the ‘European Energy Storage Technology Development Roadmap towards 2030’ (Editor: Deborah Martens [84]), which provided the following lithium-ion technology goals for 2020–2030: energy costs below 200 €  $\text{kWh}^{-1}$  with a gravimetric energy density at cell level of 180–350 Wh  $\text{kg}^{-1}$  for more than 10 000 full cycles.

Laser structuring can be applied to electrodes, separators, and current collectors. This opens up a wealth of possibilities for the evolutionary development of new battery systems with extremely high capacity and enhanced performance. For example, in the field of separator development, polyolefin separators equipped with functional coatings to stabilize SEI formation and to improve safety, are becoming increasingly important. Such novel separator foils can also be provided with 3D microstructures to improve lithium-ion diffusion and wetting. A completely new approach allows the production of self-supporting ceramic separators to further reduce the mass of inactive cell components and increase the thermal resilience and safety of battery cells.

Research in laser structuring of battery materials to improve electrolyte wetting is an approach that, so far, has only been successfully tested at the laboratory scale but shows high economic potential [16, 85]. The next evolutionary step is transferring the process to large-format cells with multiple stacks of electrodes and separators. The improvement of electrolyte wetting in cell production is an approach that can significantly reduce the production costs and failure rates of batteries. Improvements in high-rate capability, due to surface laser structuring, represent another significant up-grade in cell production, especially with regard to increases in electrode mass loading. Laser technology can be incorporated into existing production lines in a modular manner using fiber lasers, scanner technologies, and R2R processes. Scalability to large production quantities is feasible. The structuring process must be optimized with regard to increasing efficiency and process strategy. A laser system with R2R electrode feeding and high-performance fs-laser radiation meets the technological prerequisites to demonstrate the necessary transfer of laser technology to large-format cells (e.g. 40–60 Ah).

#### Acknowledgments

I am grateful to my department colleagues Heino Besser, Alexandra Reif, Peter Smyrek, Yijing Zheng, Penghui Zhu, and Alexandra Meyer for continuous technical and scientific support during electrode coating, laser materials processing, materials analytics, cell assembly, and electrochemical characterization. The research to anode material development received funding from the German Research Foundation (DFG, project No. 392322200), and the development of cathode materials and upscaling strategies was funded by the Federal Ministry of Education and Research (Project NextGen3DBat, 03XP0198F).

#### ORCID iD

Wilhelm Pflöging  <https://orcid.org/0000-0002-9221-9493>

#### References

- [1] Kwade A, Haselrieder W, Leithoff R, Modlinger A, Dietrich F and Droeder K 2018 *Nat. Energy* **3** 290
- [2] Luetke M, Franke V, Techel A, Himmer T, Klotzbach U, Wetzig A and Beyer E 2011 *Phys. Procedia* **12** 286

- [3] Helm J, Schulz A, Olowinsky A, Dohrn A and Poprawe R 2020 *Weld. World* **64** 611
- [4] Schmidt P A, Schmitz P and Zaeh M F 2016 *J. Laser Appl.* **28** 022423
- [5] Brand M J, Schmidt P A, Zaeh M F and Jossen A 2015 *J. Energy Storage* **1** 7
- [6] De Bono P and Blackburn J 2015 Laser welding of copper and aluminium battery interconnections *Industrial Laser Applications Symp. (Ilas 2015)* (International Society for Optics and Photonics) vol 9657 p 96570M
- [7] Pflöging W 2018 *Nanophotonics* **7** 549
- [8] Habedank J B, Endres J, Schmitz P, Zaeh M F and Huber H P 2018 *J. Laser Appl.* **30** 032205
- [9] Tsuda T *et al* 2018 *Electrochim. Acta* **291** 267
- [10] Park J, Hyeon S, Jeong S and Kim H-J 2019 *J. Ind. Eng. Chem.* **70** 178
- [11] Smyrek P, Pröll J, Seifert H J and Pflöging W 2016 *J. Electrochem. Soc.* **163** A19
- [12] Vedder C, Hawelka D, Wolter M, Leiva D, Stollenwerk J and Wissenbach K 2016 Laser-based drying of battery electrode layers *Int. Congress on Applications of Lasers & Electro-Optics* (Laser Institute of America) vol 2016 p N501
- [13] Broadhead J and Kuo H C 2001 Electrochemical principles and reactions *Handbook of Batteries* 3rd edn, ed D Linden (New York: McGraw-Hill) pp 2.1–37
- [14] Wang W, Wei X, Choi D, Lu X, Yang G and Sun C 2015 Electrochemical cells for medium-and large-scale energy storage: fundamentals *Advances in Batteries for Medium and Large-scale Energy Storage* (Amsterdam: Elsevier) pp 3–28
- [15] Ebner M and Wood V 2015 *J. Electrochem. Soc.* **162** A3064
- [16] Pflöging W and Pröll J 2014 *J. Mater. Chem. A* **2** 14918
- [17] Gao J, Shi S-Q and Li H 2015 *Chin. Phys. B* **25** 018210
- [18] Wu Z, Xie Z, Yoshida A, Wang Z, Hao X, Abudula A and Guan G 2019 *Renewable Sustainable Energy Rev.* **109** 367
- [19] Zhang Y, Marschilok A C, Takeuchi K J, Kercher A K, Takeuchi E S and Dudney N J 2019 *Chem. Mater.* **31** 6135
- [20] Long J W, Dunn B, Rolison D R and White H S 2004 *Chem. Rev.* **104** 4463
- [21] Ferrari S, Loveridge M, Beattie S D, Jahn M, Dashwood R J and Bhagat R 2015 *J. Power Sources* **286** 25
- [22] Serra P and Piqué A 2019 *Adv. Mater. Technol.* **4** 1800099
- [23] Zhang M, Mei H, Chang P and Cheng L 2020 *J. Mater. Chem. A* **8** 10670
- [24] Pröll J, Kim H, Piqué A, Seifert H J and Pflöging W 2014 *J. Power Sources* **255** 116
- [25] Ma L, Nie M, Xia J and Dahn J 2016 *J. Power Sources* **327** 145
- [26] Noh H J, Youn S, Yoon C S and Sun Y K 2013 *J. Power Sources* **233** 121
- [27] Bak S-M, Hu E, Zhou Y, Yu X, Senanayake S D, Cho S-J, Kim K-B, Chung K Y, Yang X-Q and Nam K-W 2014 *ACS Appl. Mater. Interfaces* **6** 22594
- [28] Obrovac M and Christensen L 2004 *Electrochem. Solid-State Lett.* **7** A93
- [29] Liang B, Liu Y and Xu Y 2014 *J. Power Sources* **267** 469
- [30] Steen M, Lebedeva N, Di Persio F and Boon-Brett L 2017 JRC Science for Policy Report (available at: <https://publications.jrc.ec.europa.eu/repository/bitstream/JRC108043/kjna28837enn.pdf>)
- [31] Roberts M *et al* 2011 *J. Mater. Chem.* **21** 9876
- [32] Li J, Daniel C and Wood D 2011 *J. Power Sources* **196** 2452
- [33] Kim H, Auyeung R C Y and Piqué A 2007 *J. Power Sources* **165** 413
- [34] Wollersheim O and Pflöging W 2012 *ATZ Elektron.* **7** 52
- [35] Wood D L, Li J L and Daniel C 2015 *J. Power Sources* **275** 234
- [36] Jaiser S, Muller M, Baunach M, Bauer W, Scharfer P and Schabel W 2016 *J. Power Sources* **318** 210
- [37] Muller M, Pfaffmann L, Jaiser S, Baunach M, Trouillet V, Scheiba F, Scharfer P, Schabel W and Bauer W 2017 *J. Power Sources* **340** 1
- [38] Yue Y and Liang H 2018 *Small Methods* **2** 1800056
- [39] Yamada M, Watanabe T, Gunji T, Wu J and Matsumoto F 2020 *Electrochem* **1** 124
- [40] Miao Y, Hynan P, von Jouanne A and Yokochi A 2019 *Energies* **12** 1074
- [41] Pagliaro M and Meneguzzo F 2019 *Heliyon* **5** e01866
- [42] Ramoni M O, Zhang Y, Zhang H-C and Ghebrab T 2017 *Int. J. Adv. Manuf. Technol.* **88** 3067
- [43] Neuenschwander B, Jaeggi B, Schmid M and Hennig G 2014 *Phys. Procedia* **56** 1047
- [44] Bolsinger M, Weller M, Ruck S, Kaya P, Riegel H and Knoblauch V 2020 *Electrochim. Acta* **330** 135163
- [45] Zhu P, Seifert H J and Pflöging W 2019 *Appl. Sci.* **9** 4067
- [46] Smyrek P, Bergfeldt T, Seifert H J and Pflöging W 2019 *J. Mater. Chem. A* **7** 5656
- [47] Ni J and Li L 2020 *Adv. Mater.* **32** 2000288
- [48] Pröll J, Kohler R, Torge M, Ulrich S, Ziebert C, Bruns M, Seifert H J and Pflöging W 2011 *Appl. Surf. Sci.* **257** 9968
- [49] Tsuda T, Ando N, Utaka T, Kojima K, Nakamura S, Hayashi N, Soma N, Gunji T, Tanabe T and Ohsaka T 2019 *Electrochim. Acta* **298** 827
- [50] Tsuda T, Ishihara Y, Watanabe T, Ando N, Gunji T, Soma N, Nakamura S, Hayashi N, Ohsaka T and Matsumoto F 2019 *Electrochemistry* **87** 370
- [51] Pflöging W and Gotcu P 2019 *Appl. Sci.* **9** 3588
- [52] Schweidler S, de Biasi L, Schiele A, Hartmann P, Brezesinski T and Janek J 2018 *J. Phys. Chem. C* **122** 8829
- [53] Dühnen S, Betz J, Kolek M, Schmuck R, Winter M and Placke T 2020 *Small Methods* **4** 2000039
- [54] Graetz J, Ahn C C, Yazami R and Fultz B 2003 *Electrochem. Solid-State Lett.* **6** A194
- [55] Kim J S, Pflöging W, Kohler R, Seifert H J, Kim T Y, Byun D, Jung H G, Choi W C and Lee J K 2015 *J. Power Sources* **279** 13
- [56] Kraft L, Habedank J B, Frank A, Rheinfeld A and Jossen A 2020 *J. Electrochem. Soc.* **167** 013506
- [57] Habedank J B, Krieglner J and Zaeh M F 2019 *J. Electrochem. Soc.* **166** A3940
- [58] Zheng Y, Seifert H J, Shi H, Zhang Y, Kübel C and Pflöging W 2019 *Electrochim. Acta* **317** 502
- [59] Shi H, Liu X, Wu R, Zheng Y, Li Y, Cheng X, Pflöging W and Zhang Y 2019 *Appl. Sci.* **9** 956
- [60] Park K-Y, Park J-W, Seong W M, Yoon K, Hwang T-H, Ko K-H, Han J-H, Jaedong Y and Kang K 2020 *J. Power Sources* **468** 228369
- [61] Mangang M, Seifert H J and Pflöging W 2016 *J. Power Sources* **304** 24
- [62] Zheng Y, Pfäffl L, Seifert H J and Pflöging W 2019 *Appl. Sci.* **9** 4218
- [63] Lai W and Ciucci F 2011 *Electrochim. Acta* **56** 4369
- [64] Mottay E, Liu X B, Zhang H B, Mazur E, Sanatinia R and Pflöging W 2016 *MRS Bull.* **41** 984
- [65] Habedank J B, Schwab D, Kiesbauer B and Zaeh M F 2020 *J. Laser Appl.* **32** 022053
- [66] Jansen T, Kandula M W, Blass D, Hartwig S, Haselrieder W and Dilger K 2020 *Energy Technol.* **8** 1900519
- [67] Lutey A H, Fortunato A, Ascari A, Carmignato S and Leone C 2015 *Opt. Laser Technol.* **65** 164
- [68] Zhang Y, Li J, Yang R, Liu T and Yan Y 2019 *Opt. Lasers Eng.* **118** 14
- [69] Du K 2008 Concepts, features, and developments of slab laser oscillators and amplifiers *Solid State Lasers XVII: Technology and Devices* (International Society for Optics and Photonics) vol 6871 p 687100
- [70] Li D and Du K 2011 Picosecond laser with 400W average power and 1mJ pulse energy *Solid State Lasers XX:*

- Technology and Devices* (International Society for Optics and Photonics) vol 7912 p 79120N
- [71] Schille J, Schneider L, Streek A, Kloetzer S and Loeschner U 2016 High-throughput machining using high average power ultrashort pulse lasers and ultrafast polygon scanner *Laser-based Micro-and Nanoprocessing X* (International Society for Optics and Photonics) vol 9736 p 97360R
- [72] Keming Du *et al* 2020 PX-SERIES (Available at: <http://www.edge-wave.de/web/en/produkte/ultra-short-pulse-systeme/px-serie/>)
- [73] Pflöging W, Kohler R, Scholz S, Ziebert C and Proell J 2011 *Spring 2011 Materials Research Society Meeting - Symposium TT: Laser-Material Interactions at Micro/Nanoscales April 2011 San Francisco* 1365 mrss11–1365
- [74] Mangang M, Pröll J, Tarde C, Seifert H J and Pflöging W 2014 *Proc. SPIE* 8968 0M1
- [75] Pröll J, Kim H, Mangang M, Seifert H J, Piqué A and Pflöging W 2014 *Proc. SPIE* 8968 051
- [76] Mangang M, Gotcu-Freis P, Seifert H J and Pflöging W 2015 *Proc. SPIE* 9351 0K1
- [77] Pröll J, Schmitz B, Niemoeller A, Robertz B, Schäfer M, Torge M, Smyrek P, Seifert H J and Pflöging W 2015 *Proc. SPIE* 9351 1F1
- [78] Smyrek P, Kim H, Zheng Y, Seifert H J, Piqué A and Pflöging W 2016 *Proc. SPIE* 9738 973806
- [79] Smyrek P, Zheng Y, Seifert H J and Pflöging W 2016 *Proc. SPIE* 9736 1C1
- [80] Pflöging W, Kohler R and Pröll J 2014 *Patent (issued)* EP 2 697 850 B1, US9337462B2, WO 2012/139553 1
- [81] Sutter D *et al* 2020 *Next generation of high-power industrial ultrafast lasers based on InnoSlab technology (Conference Presentation)* *SPIE LASE* (SPIE) <https://doi.org/10.1117/12.2544720>
- [82] Sutter D H, Dietz T, Bauer D, Scelle R, Budnicki A, Killi A, Jenne M, Kleiner J, Flamm D and Sailer M 2019 High power and high energy ultrafast disk lasers for industrial applications *CLEO: Science and Innovations* (Optical Society of America) p JM3E. 2
- [83] Schütz V, Horn A and Stute U 2012 *Proc. SPIE* 8244 82440X1
- [84] Durand J-M, Duarte M J and Clerens P 2017 European energy storage technology development roadmap towards 2030 *Int Energy Storage Policy Regul Work* vol 108 (Available at: <https://ease-storage.eu/wp-content/uploads/2015/10/EASE-EERA-recommendations-Roadmap-LR.pdf>)
- [85] Habedank J B, Günter F J, Billot N, Gilles R, Neuwirth T, Reinhart G and Zaeh M F 2019 *Int. J. Adv. Manuf. Technol.* 102 2769